Aalto University

OPEN ACCESS

This is an electronic reprint of the original article.
This reprint may differ from the original in pagination and typographic detail.

Torabi, Jalal; Niiranen, Jarkko

Microarchitecture-dependent nonlinear bending analysis for cellular plates with prismatic corrugated cores via an anisotropic strain gradient plate theory of first-order shear deformation

Published in:
Engineering Structures

DOI:
10.1016/j.engstruct.2021.112117

Published: 01/06/2021

Document Version
Publisher's PDF, also known as Version of record

Published under the following license:
CC BY-NC-ND

Please cite the original version:
Torabi, J., & Niiranen, J. (2021). Microarchitecture-dependent nonlinear bending analysis for cellular plates with prismatic corrugated cores via an anisotropic strain gradient plate theory of first-order shear deformation. *Engineering Structures*, *236*, Article 112117. https://doi.org/10.1016/j.engstruct.2021.112117

This material is protected by copyright and other intellectual property rights, and duplication or sale of all or part of any of the repository collections is not permitted, except that material may be duplicated by you for your research use or educational purposes in electronic or print form. You must obtain permission for any other use. Electronic or print copies may not be offered, whether for sale or otherwise to anyone who is not an authorised user.

Engineering Structures 236 (2021) 112117

Contents lists available at ScienceDirect

Engineering Structures

journal homepage: www.elsevier.com/locate/engstruct

Microarchitecture-dependent nonlinear bending analysis for cellular plates with prismatic corrugated cores via an anisotropic strain gradient plate theory of first-order shear deformation

Jalal Torabi *, Jarkko Niiranen

Department of Civil Engineering, School of Engineering, Aalto University, P.O. Box 12100, Aalto 00076, Finland

ARTICLE INFO

Keywords:
Cellular plates
Anisotropic strain gradient plate model
Nonlinear bending analysis
C^1-continuous finite element
Triangular prismatic microarchitecture

ABSTRACT

This study focuses on the microarchitecture-dependent nonlinear bending behavior of cellular plates with equitriangularly prismatic microarchitectures by adopting a dimensionally and constitutively reduced strain gradient plate model. The strain energy formulation is based on the dimension reduction of the first-order shear deformation plate theory along with von Kármán's nonlinear strain relations and anisotropic strain gradient theory. The classical and higher-order constitutive parameters are obtained according to the recently published homogenization results for a corresponding linear plate model. The corresponding finite element simulations, numerically solving the anisotropic strain gradient plate problems, rely on a nonstandard, higher-order, six-node triangular element showing good convergence properties. Comparisons between the proposed (2D) strain gradient shear deformation plate model and the corresponding (3D) detailed full-field reference models demonstrate for a variety of cellular plate structures that the accuracy of the proposed approach is at a very good level with relatively low computational costs. A diverse set of numerical examples is provided in order to investigate the size-dependent nonlinear structural response of cellular plates having different numbers of microarchitectural layers, midsurface shapes and boundary conditions.

1. Introduction

Owing to vast improvements in design and manufacturing technologies and remarkable mechanical properties, a large variety of applications of advanced cellular metamaterials in various science and engineering fields have been developed [1–3]. Based on different design aspects such as shape, size and topology, cellular structures with different microarchitectures can be extensively used in a variety of industrial applications such as lightweight components, absorbers and dampers [4–6]. Hence, providing efficient theoretical and computational infrastructures for predicting the material properties and mechanical behavior of lattice metamaterials play an important role in the work flow of accurate and efficient structural design. However, due to the high computational costs [7,8] and intricate microarchitecture-dependent mechanical characteristics [9–12], the structural modeling of lattice metamaterials is a complex and time-consuming task for engineers and scholars.

The classical continuum mechanics can be effectively employed to study the physics and mechanics of a diverse range of materials and metamaterials. However, especially for (a) small-scale structures and (b) structures of any scale with a microarchitecture more general but still practical and efficient approaches should be employed for considering additional aspects such as size effects. In (a), a (natural) material microstructure affects the structural behavior, whereas in (b) the structural behavior is affected by a certain (artificial) metamaterial microarchitecture. This way, independently of the physical scale, there are typically two neighboring scales for which the principle of separation of scales is not fully valid. In the present study belonging to the line (b) when it comes to applications, the structural scale describes the overall structure (e.g., a plate), whereas the microarchitectural scale defines the internal configurations (e.g., the geometric details of a unit cell of a periodic honeycomb structure). The higher-order continuum theories such as microcontinuum theory [13,14] (including micropolar, microstretch and micromorphic theories), nonlocal theory [15–18] and strain gradient theory (SGT) [19–23] provide efficient models for the incorporation of more than one scale and, accordingly, for capturing size effects in structural modeling. The fundamental principle in the generalized continuum theories is to provide a physico-mathematical

* Corresponding author.
E-mail address: jalal.torabi@aalto.fi (J. Torabi).

https://doi.org/10.1016/j.engstruct.2021.112117
Received 5 October 2020; Received in revised form 19 February 2021; Accepted 23 February 2021
Available online 15 March 2021
0141-0296/© 2021 The Author(s). Published by Elsevier Ltd. This is an open access article under the CC BY-NC-ND license (http://creativecommons.org/licenses/by-nc-nd/4.0/).

description richer than the classical Cauchy's continuum framework but to keep as much as possible of the generality, applicability and relative simplicity implied by the fundamental continuum assumptions and the rigorous mathematicality. On one hand, the generalized theories enable to describe some essential physical phenomena, e.g., size-effects, overlooked by the classical continuum theory. On the other hand, the non-physical stress singularities present in the classical theory of elasticity, for instance, do not appear in the strain gradient theory of elasticity. For further discussion, a detailed and informative review study on beam and plate models within these non-classical theories can be found in [24].

Although a diverse variety of investigations based on the non-classical continuum theories can be found in the literature [25–32], the SGT seems to be the most commonly studied theory for investigating the size-dependent physicomechanical behavior of nano/micro-scale structures and macro-scale (or any-scale) structures with architected microstructures. Connected to the present study, the classical Kirchhoff plate models within the (different versions of the) SGT were first presented by Yang et al. [33], Lazopoulos [34,35], Beskou and Beskos [36], Wang et al. [37] as well as Movassagh and Mahmoodi [38]. The applications of the first-order and higher-order shear deformation theory (FSDT and HSDT) for structural analysis of beams, plates and shells under the classical continuum theories have been extensively demonstrated in the literature [39–46], howevere, the implementation of the FSDT for plates within the SGT was first studied by Ramezani [47]. Niiranen et al. presented a variational formulation [48] and isogeometric analysis [49] for strain gradient Kirchhoff plates. Thai et al. [50] also dealt with the static and dynamic isogeometric analysis of functionally graded microplates under the modified SGT. The size-dependent buckling and wave propagation analysis of functionally graded nanoplates and shells were presented by Karami et al. [51,52] following the nonlocal SGT. Higher-order three-node triangular [53] 2D finite element (FE) was introduced by Ansari and his co-authors to numerically model the linear vibration of microplates. A nonlinear FE formulation for the three-dimensional strain gradient theory was formulated by Torabi et al. [54] and two higher-order 3D elements were proposed and applied to plate problems [54,55]. In addition, nonlinear finite element electro-magneto-mechanical analysis of microbeam under the modified SGT was presented by Alimirzaei et al. [56]. A strain gradient Kirchhoff–Love shell model with an isogeometric FE study was developed by Balobanov et al. [57]. More numerical studies on the strain gradient problems can be found in [58–63].

Although various studies on the structural behavior of sandwich lattice structures can be found under the classical continuum theories [45,46,64–67], the literature on the microarchitecture-dependent mechanical modeling of lattice or cellular structures, or mechanical metamaterials, within the generalized continuum theories is fairly limited [7,9,11,12,26,59,68–82]. Connected to the present study, for the so-called pantographic structures there exists a fairly solid theoretical understanding [9,11] and a variety of numerical and experimental validation studies [12]. Auffray et al. [69] developed a strain gradient homogenization approach for 2D cellular media. Khakalo et al. [70,71] presented a detailed study on the size-dependent modeling of uniform and functionally graded 2D equitriangular (stretching-dominated) multi-layer lattice beams under the SGT: the two standard variants of the first-order beam kinematics, typically called the Bernoulli–Euler or engineering beam model and the Timoshenko or first-order shear deformation beam model, were considered, and a computational homogenization method was employed to determine the non-classical material parameters. An extension to the geometrically nonlinear regime was accomplished by Tran and Niiranen [73]. A comparative study for 2D square multi-layer lattice beam has been accomplished very recently in [74], whereas for modeling single-layer web-core sandwich structures, sharing essentially the same (bending-dominated) lattice geometry, the modified couple stress Timoshenko beam theory was applied by Romanoff and Reddy [75]. Réthoré et al. [76] focused on the validation and identification study of honeycomb architectures from full-field experimental measurements. A numerical study on the topology optimization of lattice structures, by adopting the SGT with a non-local numerical homogenization technique, was presented by Da et al. [77]. Very recently, Chowdhury and Reddy [79] presented a micropolar Timoshenko beam formulation for sandwich beams with architected lattice cores. Karttunen et al. [80] and Nampally et al. [81] focused on the development of a two-scale constitutive model for lattice core sandwich beams based on the micropolar theory. Besides, linear and geometrically nonlinear micropolar plate models were developed in [82,83] for the bending analysis of lattice core sandwich structures. Although [82,83] focus on modeling single-layer sandwich structures and rely on the micropolar theory, the section for conclusions and discussion in the end of the present article address some natural links between those studies and the present study which, in turn, relies on the SGT and aims at capturing the bending size effect observed in multi-layer (metamaterial) sandwich structures. In this context, it is still worth mentioning that in the vastly growing literature on generalized continuum theories, largely inspired by certain experimental observations for small-scale structures nearly 20 years ago (e.g., [21]), model validation seems to play a minor role – although some results from micro- or nano-scale experiments and molecular dynamics simulations are available as reviewed in [24]. Structures having a (man-made) microarchitecture offer, however, a natural option for model validation – not only through laboratory experiments at different scales [12,75,84] but through virtual experiments as well [7,12,70–83]: via analytical or computational homogenization relying on a set of given base material properties and reference models depicting every little detail of micro-architectural geometries (as illustrated in Fig. 1, left). Additive manufacturing technologies, in particular, have paved the way to realize the corresponding laboratory experiments and it is expected to enable the production of future industrial applications of microarchitectural structures [84] – such as the multi-layer (metamaterial) sandwich structures considered in the present study. In the end, the development of multi-scale continuum models and solution methods for different microarchitectures gains quite general knowledge for the modeling of the somewhat analogous microstructural phenomena related to natural engineering materials.

Although web core sandwich plates (typical in many industrial applications of today) can be seen as plate structures including single-layer lattice geometries – such structures been studied by classical (see, e.g., the review in [1]) and generalized [82,83] continuum models – the study of Khakalo and Niiranen [7] seems to be an exception focusing on multi-layer structures made of a periodic lattice which can be identified as a metamaterial: the article formulates anisotropic plate models following the Kirchhoff and FSDT theories within the thermomechanical SGT and proposes numerical homogenization procedures for the determination of the corresponding classical and higher-order constitutive parameters for multi-layer cellular plates having equitriangularly prismatic corrugated cores (as illustrated in Fig. 1, left, for one-, two- and three-layer structures as examples). It is crucial to notice, first, that the plate model (Fig. 1, right) sees the underlying equitriangularly prismatic configuration (further illustrated in Fig. 2 (I) in Section 2), made of a classical elastic base material, as a three-dimensional metamaterial with a representative unit cell (Fig. 2 (II) and (III)) and certain periodicity: stacking layers on top of each other, leads to a honeycomb structure with constant and uniform wall thickness, i.e., a homogeneous metamaterial. Second, by relying on the classical computational homogenization principles, the effective classical material properties following the three-dimensional transversal isotropy can be obtained. Third, and most importantly, a size effect comes into the picture when analyzing the bending of thin plate structures made of this metamaterial (see Fig. 1, left): the size of the unit cell becomes comparable to the thickness of the structure for small number of layers (cf. microplates made of natural materials; case (a) above). Classical unisotropic plate models, dimensionally reduced from the classical three-dimensional continuum description with the material matrix of a proper transversal isotropy, do

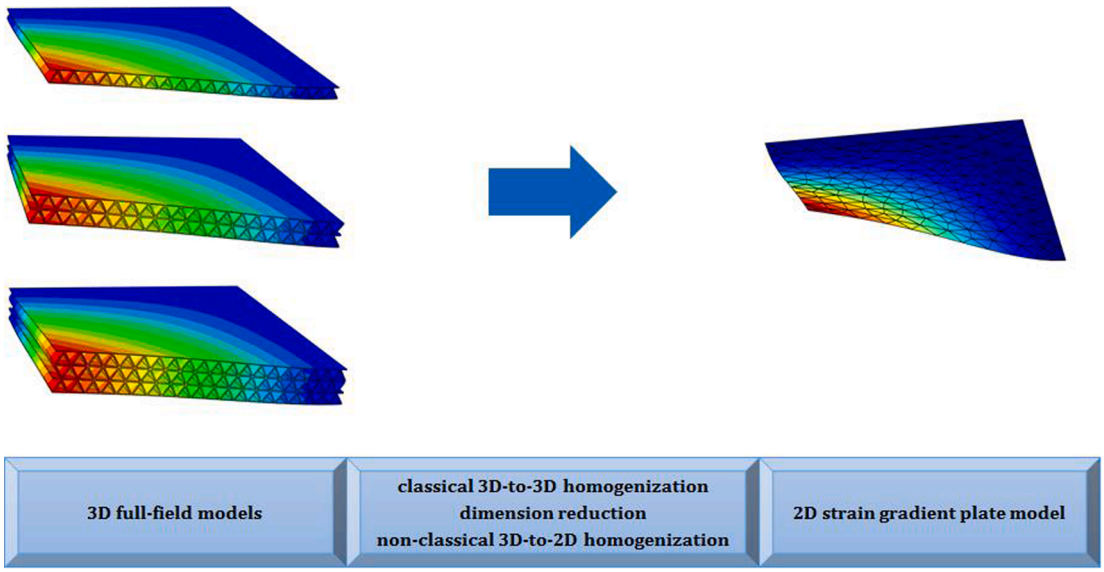

Fig. 1. The fundamental idea for the employment of classical and generalized homogenization techniques based on the three-dimensional classical and strain gradient elasticity to develop a computationally efficient model for capturing the bending size effect of cellular plate structures.

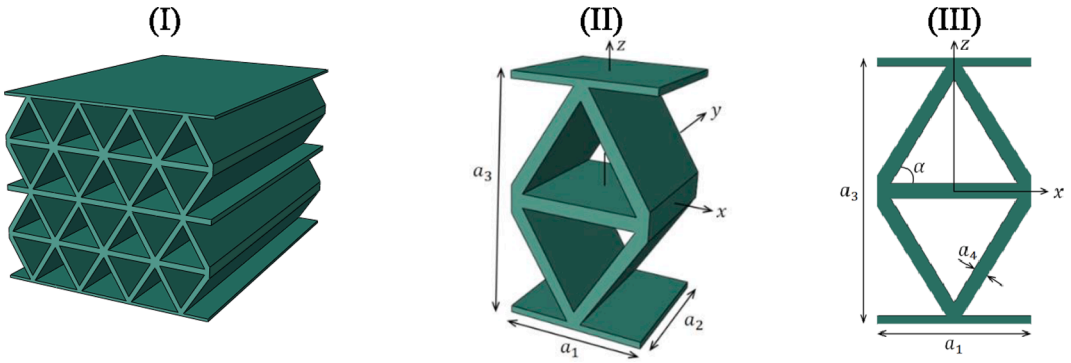

Fig. 2. Schematic views of the triangularly cellular metamaterial (I) and the corresponding geometrical parameters of a unit cell (II and III).

not capture the bending bahavior of plates having only a few layers of triangles in the thickness direction. More precisely, with less than eight triangles in the thickness direction, error levels varied from a few percent to tens of percent within linear elasticity [7]. The corresponding strain gradient plate models, however, were shown to capture the size effect for linearly elastic structures: the generalized models correctly described the transition from the strongly non-classical bending behavior (of plates with one or two triangles in the thickness direction) to mildly non-classical and classical behavior (according to the increase in the number of triangles). Motivated by these results, the present study investigates the size effect of similar multi-layer cellular plates but within the geometrically nonlinear regime, coupling the bending and membrane states, by further developing the anisotropic plate model of the FSDT within the SGT. In addition, instead of adopting the conforming isogeometric (NURBS-based) FE method of [7] (having certain well-known practical restrictions), a quasi-conforming isoparametric (polynomial) FE method is introduced, implemented, verified and finally applied in the corresponding model validation.

This article provides the following novel content: (1) a derivation for a geometrically nonlinear strain gradient plate model, coupling the bending and membrane states, with an application to multi-layer cellular plates; (2) the development of a quasi-C^1-conforming 6-node triangular finite element; (3) a numerical method verification for the new finite element; (4) a numerical model validation for the new plate model. An appropriate strain energy functional is derived in Section 2 by following the anisotropic SGT and FSDT in conjunction with the von Kármán geometric nonlinearity. The anisotropic classical and strain gradient material properties for the bending terms of the plate model are taken from [7] and then modified for the stretching and mixed (bending-stretching) terms of the nonlinear formulation. Then, in order to to numerically analyze plates with various shapes and boundary conditions, a corresponding FE formulation and a quasi-C^1-continuous six-node triangular element are introduced in Section 3.

In Section 4, convergence studies first confirm the reliability of the element. For the purposes of model validation, a (3D) full-field model of geometrically nonlinear classical elasticity – accounting for the geometric details of the chosen cellular structures – is compared to the (2D) strain gradient plate model in order to investigate the accuracy of the proposed size-dependent but dimensionally reduced non-classical model. Finally, a diverse set of numerical examples for equitriangularly prismatic cellular plates with various shapes (rectangular, skew, circular, elliptical, annular sector and polygon) and combinations of boundary conditions is presented for analyzing the microarchitecture-induced size effects in the nonlinear bending response of such structures.

2. Anisotropic strain gradient plate model

2.1. Mindlin's strain gradient theory of elasticity

Based on Mindlin's SGT of elasticity [19], the functional of strain

energy is expressed on the basis of the classical strain and stress tensors (ε_{ij},S_{ij}), and (non-classical) strain gradient and double stress tensors (κ_{ijk}, τ_{ijk}) as

$$\mathscr{F} = \int_V (S_{ij}\varepsilon_{ij} + \tau_{ijk}\kappa_{ijk})dV \tag{1}$$

where V denotes the occupied volume of a three-dimensional solid body. The components of the nonlinear strain and strain gradient tensors are presented as

$$\varepsilon_{ij} = \frac{1}{2}\left(u_{i,j} + u_{j,i} + u_{k,i}u_{k,j}\right) = \varepsilon_{ji}, \kappa_{ijk} = \varepsilon_{ij,k} = \kappa_{jik} \tag{2}$$

where u_i denotes the displacement along the coordinate direction i and the comma in the subscript stands for the differentiation in the coordinate direction indicated by the subsequent subscript index. The conjugate variables for the strain and strain gradient, respectively, are given by the classical and higher-order constitutive relations for the stress and double stress tensors as follows:

$$S_{ij} = C_{ijkl}\varepsilon_{kl} \tag{3}$$

$$\tau_{ijk} = A_{ijklmn}\kappa_{lmn} \tag{4}$$

where C_{ijkl} and A_{ijklmn} denote the classical fourth-order stiffness tensor and a (non-classical) sixth-order stiffness tensor, respectively. More details on the fundamentals of the SGT can be found in [7,34,47]. The strain gradient formulation following the nonlinear FSDT of plates is provided in the next section: the corresponding kinematical assumption is inserted into the three-dimensional energy formulation described by (1)–(4).

2.2. First-order shear deformation plate model

As explained in the Introduction, our final aim is to model plate-like cellular structures (see Fig. 1) made from a metamaterial formed by repeating the geometry of a triangular unit cell as the example one depicted in Fig. 2. For this purpose, we next derive a geometrically nonlinear FSDT plate model within the strain gradient theory of elasticity briefly recalled in the previous Section 2.1. Within the derivation of the model, we address the crucial differences between the classical and strain gradient FSDT plates. These differences, first, bring a size dependency into the model and, second, require a nonstandard FE formulation due to the higher-order gradients involved in the model.

The fundamental equations on the strain–displacement and constitutive relations, and the corresponding strain energy functional, are derived in this section for the nonlinear strain gradient FSDT of plates by adopting von Kármán's nonlinear kinematic relations. First, by considering u_x, u_y, u_z and θ_x,θ_y, respectively, as the displacements and rotations of the mid-plane of a plate structure and by the use of the Cartesian coordinate system of (x,y,z), the nonlinear strain components read as

$$\boldsymbol{\varepsilon} = \begin{Bmatrix} \boldsymbol{\varepsilon}_1 \\ \boldsymbol{\varepsilon}_2 \end{Bmatrix}$$

$$\boldsymbol{\varepsilon}_1 = \begin{Bmatrix} \varepsilon_{xx} \\ \varepsilon_{yy} \\ \gamma_{xy} \end{Bmatrix} = \begin{Bmatrix} u_{x,x} \\ u_{y,y} \\ u_{x,y} + u_{y,x} \end{Bmatrix} + 1/2 \begin{Bmatrix} u_{z,x}^2 \\ u_{z,y}^2 \\ 2u_{z,x}u_{z,y} \end{Bmatrix} + z \begin{Bmatrix} \theta_{x,x} \\ \theta_{y,y} \\ \theta_{x,y} + \theta_{y,x} \end{Bmatrix} \tag{5}$$

$$\boldsymbol{\varepsilon}_2 = \begin{Bmatrix} \gamma_{xz} \\ \gamma_{yz} \end{Bmatrix} = \begin{Bmatrix} \theta_x + u_{z,x} \\ \theta_y + u_{z,y} \end{Bmatrix}$$

where $\boldsymbol{\varepsilon}_1$ and $\boldsymbol{\varepsilon}_2$ are the vectors of in-plane (membrane and bending) and transverse (shear) strains, respectively. By introducing the following linear ($\mathbf{E}_1$,$\mathbf{E}_2$) and nonlinear ($\mathbf{E}_n$) matrix operators

$$\mathbf{E}_1 = \begin{bmatrix} \partial/\partial x & 0 & 0 & 0 & 0 \\ 0 & \partial/\partial y & 0 & 0 & 0 \\ \partial/\partial y & \partial/\partial x & 0 & 0 & 0 \\ 0 & 0 & 0 & \partial/\partial x & 0 \\ 0 & 0 & 0 & 0 & \partial/\partial y \\ 0 & 0 & 0 & \partial/\partial y & \partial/\partial x \end{bmatrix}, \ \mathbf{E}_2 = \begin{bmatrix} 0 & 0 & \partial/\partial x & 1 & 0 \\ 0 & 0 & \partial/\partial y & 0 & 1 \end{bmatrix}$$

$$\mathbf{E}_n = \langle \mathbf{G}_1\mathbf{d}\rangle\mathbf{G}_2 + \langle \mathbf{G}_2\mathbf{d}\rangle\mathbf{G}_1$$

$$\mathbf{G}_1 = \begin{bmatrix} \partial/\partial x \\ \partial/\partial y \\ \partial/\partial x \end{bmatrix} \otimes [0 \ \ 0 \ \ 1 \ \ 0 \ \ 0], \ \mathbf{G}_2 = \frac{1}{2}\begin{bmatrix} \partial/\partial x \\ \partial/\partial y \\ 2\partial/\partial y \end{bmatrix} \otimes [0 \ \ 0 \ \ 1 \ \ 0 \ \ 0], \tag{6}$$

the strain vectors can be expressed as

$$\boldsymbol{\varepsilon}_1 = \left(\mathbf{L}_1\mathbf{E}_1 + \frac{1}{2}\mathbf{E}_n\right)\mathbf{d}, \boldsymbol{\varepsilon}_2 = \mathbf{E}_2\mathbf{d} \tag{7}$$

where $\mathbf{d} = \left[u_x u_y u_z \theta_x \theta_y\right]^{\mathrm{T}}$ stands for the displacement vector and $\mathbf{I}_{3\times3}$ in $\mathbf{L}_1 = [\mathbf{I}_{3\times3} \ \ z\mathbf{I}_{3\times3}]$ denotes an identity matrix. Note that $\langle\rangle$ symbolizes the diag function and the symbol $\otimes$ stands for the Kronecker product.

Next, in accordance with the strain gradient relation in Eq. (2) and by following the proposed strain vectors in Eq. (5), the strain gradient vector is expressed as

$$\boldsymbol{\kappa} = \begin{Bmatrix} \boldsymbol{\kappa}_1 \\ \boldsymbol{\kappa}_2 \\ \boldsymbol{\kappa}_3 \\ \boldsymbol{\kappa}_4 \end{Bmatrix}, \tag{8}$$

$$\begin{aligned} \boldsymbol{\kappa}_1 &= \begin{Bmatrix} \kappa_{xxx} \\ \kappa_{yyx} \\ \kappa_{yxy} \end{Bmatrix} = \begin{Bmatrix} \varepsilon_{xx,x} \\ \varepsilon_{yy,x} \\ \gamma_{yx,y} \end{Bmatrix} \\ &= \begin{Bmatrix} u_{x,xx} \\ u_{y,xy} \\ u_{x,yy} + u_{y,xy} \end{Bmatrix} + \begin{Bmatrix} u_{z,x}u_{z,xx} \\ u_{z,y}u_{z,xy} \\ u_{z,x}u_{z,yy} + u_{z,y}u_{z,xy} \end{Bmatrix} + z\begin{Bmatrix} \theta_{x,xx} \\ \theta_{y,xy} \\ \theta_{x,yy} + \theta_{y,xy} \end{Bmatrix}, \end{aligned} \tag{9}$$

$$\begin{aligned} \boldsymbol{\kappa}_2 &= \begin{Bmatrix} \kappa_{yyy} \\ \kappa_{xxy} \\ \kappa_{xyx} \end{Bmatrix} = \begin{Bmatrix} \varepsilon_{yy,y} \\ \varepsilon_{xx,y} \\ \gamma_{xy,x} \end{Bmatrix} \\ &= \begin{Bmatrix} u_{y,yy} \\ u_{x,xy} \\ u_{x,xy} + u_{y,xx} \end{Bmatrix} + \begin{Bmatrix} u_{z,y}u_{z,yy} \\ u_{z,x}u_{z,xy} \\ u_{z,y}u_{z,xx} + u_{z,x}u_{z,xy} \end{Bmatrix} + z\begin{Bmatrix} \theta_{y,yy} \\ \theta_{x,xy} \\ \theta_{x,xy} + \theta_{y,xx} \end{Bmatrix}, \end{aligned} \tag{10}$$

$$\begin{aligned} \boldsymbol{\kappa}_3 &= \begin{Bmatrix} \kappa_{xxz} \\ \kappa_{xzx} \\ \kappa_{yyz} \\ \kappa_{yzy} \end{Bmatrix} = \begin{Bmatrix} \varepsilon_{xx,z} \\ \gamma_{xz,x} \\ \varepsilon_{yy,z} \\ \gamma_{yz,y} \end{Bmatrix} = \begin{Bmatrix} \theta_{x,x} \\ \theta_{x,x} + u_{z,xx} \\ \theta_{y,y} \\ \theta_{y,y} + u_{z,yy} \end{Bmatrix}, \boldsymbol{\kappa}_4 = \begin{Bmatrix} \kappa_{xyz} \\ \kappa_{yzx} \\ \kappa_{zxy} \end{Bmatrix} = \begin{Bmatrix} \gamma_{xy,z} \\ \gamma_{yz,x} \\ \gamma_{zx,y} \end{Bmatrix} \\ &= \begin{Bmatrix} \theta_{x,y} + \theta_{y,x} \\ \theta_{y,x} + u_{z,xy} \\ \theta_{x,y} + u_{z,xy} \end{Bmatrix} \end{aligned} \tag{11}$$

It should be noticed here that the derivatives of displacement and rotation components of strain gradients $\boldsymbol{\kappa}_1$ and $\boldsymbol{\kappa}_2$ are of a higher order, which holds true for some of the components of $\boldsymbol{\kappa}_3$ and $\boldsymbol{\kappa}_4$ as well. The strain gradient components of $\boldsymbol{\kappa}_3$ and $\boldsymbol{\kappa}_4$ in (11) having z as the last subscript produce the most crucial terms of the formulation, however: z as the last subscript, meaning differentiating with respect to z, results in first-order derivatives of rotation components (e.g, $\theta_{x,x}$ in $\boldsymbol{\kappa}_3$) which are analogous to the ones of strain $\boldsymbol{\varepsilon}_1$ in (5) (including, e.g, $\theta_{x,x}$) but in (11) they appear without z as a multiplier. The crucial implication of this will be further addressed in what follows.

By introducing the linear matrix operators (analogous to $\mathbf{E}_1$ and $\mathbf{E}_2$

above including first-order partial derivatives)

$$\mathbf{H}_1 = \begin{bmatrix} \partial^2/\partial x^2 & 0 & 0 & 0 & 0 \\ 0 & \partial^2/\partial x\partial y & 0 & 0 & 0 \\ \partial^2/\partial y^2 & \partial^2/\partial x\partial y & 0 & 0 & 0 \\ 0 & 0 & \partial^2/\partial x^2 & 0 & 0 \\ 0 & 0 & 0 & 0 & \partial^2/\partial x\partial y \\ 0 & 0 & \partial^2/\partial y^2 & 0 & \partial^2/\partial x\partial y \end{bmatrix}, \tag{12}$$

$$\mathbf{H}_2 = \begin{bmatrix} 0 & \partial^2/\partial y^2 & 0 & 0 & 0 \\ \partial^2/\partial x\partial y & 0 & 0 & 0 & 0 \\ \partial^2/\partial x\partial y & \partial^2/\partial x^2 & 0 & 0 & 0 \\ 0 & 0 & 0 & 0 & \partial^2/\partial y^2 \\ 0 & 0 & 0 & \partial^2/\partial x\partial y & 0 \\ 0 & 0 & 0 & \partial^2/\partial x\partial y & \partial^2/\partial x^2 \end{bmatrix},$$

$$\mathbf{H}_3 = \begin{bmatrix} 0 & 0 & 0 & \partial/\partial x & 0 \\ 0 & 0 & \partial^2/\partial x^2 & \partial/\partial x & 0 \\ 0 & 0 & 0 & 0 & \partial/\partial y \\ 0 & 0 & \partial^2/\partial y^2 & 0 & \partial/\partial y \end{bmatrix}, \mathbf{H}_4 = \begin{bmatrix} 0 & 0 & 0 & \partial/\partial y & \partial/\partial x \\ 0 & 0 & \partial^2/\partial x\partial y & 0 & \partial/\partial x \\ 0 & 0 & \partial^2/\partial x\partial y & \partial/\partial y & 0 \end{bmatrix}$$

and the nonlinear operators (analogous to $\mathbf{E}_n$ and $\mathbf{G}_i$bove including first-order partial derivatives)

$$\mathbf{H}_n = \langle \mathbf{Q}_1\mathbf{d}\rangle\mathbf{Q}_2 + \langle \mathbf{Q}_2\mathbf{d}\rangle\mathbf{Q}_1, \overline{\mathbf{H}}_n = \langle \mathbf{Q}_3\mathbf{d}\rangle\mathbf{Q}_4 + \langle \mathbf{Q}_4\mathbf{d}\rangle\mathbf{Q}_3,$$

$$\mathbf{Q}_1 = \begin{bmatrix} \dfrac{\partial}{\partial x} \\ \dfrac{\partial}{\partial y} \\ \partial/\partial x \\ \dfrac{\partial}{\partial y} \end{bmatrix} \otimes [0\ \ 0\ \ 1\ \ 0\ \ 0], \mathbf{Q}_2 = \begin{bmatrix} \partial^2/\partial x^2 \\ \partial^2/\partial x\partial y \\ \partial^2/\partial y^2 \\ \partial^2/\partial x\partial y \end{bmatrix} \otimes [0\ \ 0\ \ 1\ \ 0\ \ 0],$$

$$\mathbf{Q}_3 = \begin{bmatrix} \partial/\partial y \\ \partial/\partial x \\ \partial/\partial y \\ \partial/\partial x \end{bmatrix} \otimes [0\ \ 0\ \ 1\ \ 0\ \ 0], \mathbf{Q}_4 = \begin{bmatrix} \partial^2/\partial y^2 \\ \partial^2/\partial x\partial y \\ \partial^2/\partial x^2 \\ \partial^2/\partial x\partial y \end{bmatrix} \otimes [0\ \ 0\ \ 1\ \ 0\ \ 0], \tag{13}$$

the strain gradient vectors given in Eqs. (9)–(11) are rewritten as follows:

$$\boldsymbol{\kappa}_1 = \left(\mathbf{L}_1\mathbf{H}_1 + \frac{1}{2}\mathbf{L}_2\mathbf{H}_n\right)\mathbf{d}, \boldsymbol{\kappa}_2 = \left(\mathbf{L}_1\mathbf{H}_2 + \frac{1}{2}\mathbf{L}_2\overline{\mathbf{H}}_n\right)\mathbf{d}, \boldsymbol{\kappa}_3 = \mathbf{H}_3\mathbf{d}, \boldsymbol{\kappa}_4 = \mathbf{H}_4\mathbf{d}, \tag{14}$$

in which one has

$$\mathbf{L}_2 = \begin{bmatrix} 1 & 0 & 0 & 0 \\ 0 & 1 & 0 & 0 \\ 0 & 0 & 1 & 1 \end{bmatrix} \tag{15}$$

In addition, by using the Voigt notation in the constitutive relations of Eqs. (3) and (4) and by following the strain and strain gradient vectors of Eq. (5) and (8)–(11), respectively, the classical and higher-order stress vectors are expressed by the following relations:

$$\mathbf{S} = \begin{Bmatrix} \mathbf{S}_1 \\ \mathbf{S}_2 \end{Bmatrix} = \begin{bmatrix} \mathcal{C}_1 & 0 \\ 0 & \mathcal{C}_2 \end{bmatrix} \begin{Bmatrix} \boldsymbol{\varepsilon}_1 \\ \boldsymbol{\varepsilon}_2 \end{Bmatrix} \tag{16}$$

$$\boldsymbol{\tau} = \begin{Bmatrix} \boldsymbol{\tau}_1 \\ \boldsymbol{\tau}_2 \\ \boldsymbol{\tau}_3 \\ \boldsymbol{\tau}_4 \end{Bmatrix} = \begin{bmatrix} \mathcal{A}_1 & \mathbf{0} & \mathbf{0} & \mathbf{0} \\ \mathbf{0} & \mathcal{A}_2 & \mathbf{0} & \mathbf{0} \\ \mathbf{0} & \mathbf{0} & \mathcal{A}_3 & \mathbf{0} \\ \mathbf{0} & \mathbf{0} & \mathbf{0} & \mathcal{A}_4 \end{bmatrix} \begin{Bmatrix} \boldsymbol{\kappa}_1 \\ \boldsymbol{\kappa}_2 \\ \boldsymbol{\kappa}_3 \\ \boldsymbol{\kappa}_4 \end{Bmatrix} \tag{17}$$

in which one has the in-plane (x, y) and transverse (z) stress contributions

$$\mathbf{S}_1 = \begin{Bmatrix} S_{xx} \\ S_{yy} \\ S_{xy} \end{Bmatrix}, \mathbf{S}_2 = \begin{Bmatrix} S_{xz} \\ S_{yz} \end{Bmatrix}, \mathcal{C}_1 = \begin{bmatrix} \mathscr{C}_{11} & \mathscr{C}_{12} & 0 \\ \mathscr{C}_{22} & 0 & \\ \mathscr{C}_{66} & & \end{bmatrix}, \mathcal{C}_2 = \begin{bmatrix} \mathscr{C}_{55} & 0 \\ 0 & \mathscr{C}_{44} \end{bmatrix} \tag{18}$$

for the classical stresses, with the corresponding classical material parameters of anisotropy organized in $\mathcal{C}_1$, and $\mathcal{C}_2$, respectively, whereas the corresponding higher-order stress quantities are given as

$$\boldsymbol{\tau}_1 = \begin{Bmatrix} \tau_{xxx} \\ \tau_{yyx} \\ \tau_{yxy} \end{Bmatrix}, \boldsymbol{\tau}_2 = \begin{Bmatrix} \tau_{yyy} \\ \tau_{xxy} \\ \tau_{xyx} \end{Bmatrix}, \boldsymbol{\tau}_3 = \begin{Bmatrix} \tau_{xxz} \\ \tau_{xzx} \\ \tau_{yyz} \\ \tau_{yzy} \end{Bmatrix}, \boldsymbol{\tau}_4 = \begin{Bmatrix} \tau_{xyz} \\ \tau_{yzx} \\ \tau_{zxy} \end{Bmatrix}, \tag{19}$$

$$\mathcal{A}_1 = \begin{bmatrix} c^1_{11} & c^1_{12} & c^1_{13} \\ c^1_{22} & c^1_{23} & \\ c^1_{33} & & \end{bmatrix}, \mathcal{A}_2 = \begin{bmatrix} c^2_{11} & c^2_{12} & c^2_{13} \\ c^2_{22} & c^2_{23} & \\ c^2_{33} & & \end{bmatrix}, \mathcal{A}_3 = \begin{bmatrix} c^3_{11} & c^3_{12} & c^3_{13} & c^3_{14} \\ c^3_{22} & c^3_{23} & c^3_{24} & \\ c^1_{33} & c^3_{34} & & \\ c^3_{44} & & & \end{bmatrix}, \mathcal{A}_4 = \begin{bmatrix} c^4_{11} & c^4_{12} & c^4_{13} \\ c^1_{22} & c^4_{23} & \\ c^4_{33} & & \end{bmatrix} \tag{20}$$

with the corresponding non-classical (strain gradient) material parameters organized in $\mathcal{A}_i$. It should be noticed that the higher-order stress components in $\boldsymbol{\tau}_3$ and $\boldsymbol{\tau}_4$ with z as the last subscript are connected to the most crucial terms of the formulation as addressed above and in what follows.

2.3. Principle of virtual work

By considering W as the work done by the external forces and $\mathscr{T}$ as the total strain energy, the principle of virtual work is given as $\delta\mathscr{T} + \delta W = 0$ where δ denotes the first variation. In accordance with the proposed relations for the strain, stress, strain gradient and double stress vectors, the first variation of the total strain energy reads as

$$\delta\mathscr{T} = \int_V \left(\delta\boldsymbol{\varepsilon}^{\mathrm{T}}\mathbf{S} + \delta\boldsymbol{\kappa}^{\mathrm{T}}\boldsymbol{\tau}\right)dV = \int_V \left(\delta\boldsymbol{\varepsilon}_1^{\mathrm{T}}\mathcal{C}_1\boldsymbol{\varepsilon}_1 + \delta\boldsymbol{\varepsilon}_2^{\mathrm{T}}\mathcal{C}_2\boldsymbol{\varepsilon}_2 + \sum_{m=1}^{4}\delta\boldsymbol{\kappa}_{\mathrm{m}}^{\mathrm{T}}\mathcal{A}_{\mathrm{m}}\boldsymbol{\kappa}_{\mathrm{m}}\right)dV \tag{21}$$

By taking the linear and nonlinear operators defined in Eqs. (6), (12) and (13) and according to Eqs. (7) and (14), the first variation of the ($\boldsymbol{\varepsilon}_1$ and $\boldsymbol{\varepsilon}_2$) strain and strain gradient vectors ($\boldsymbol{\kappa}_1$, $\boldsymbol{\kappa}_2$, $\boldsymbol{\kappa}_3$ and $\boldsymbol{\kappa}_4$) are given as

$$\delta\boldsymbol{\varepsilon}_1 = (\mathbf{L}_1\mathbf{E}_1 + \mathbf{E}_n)\delta\mathbf{d}, \delta\boldsymbol{\varepsilon}_2 = \mathbf{E}_2\delta\mathbf{d}, \tag{22}$$

$$\delta\boldsymbol{\kappa}_1 = (\mathbf{L}_1\mathbf{H}_1 + \mathbf{L}_2\mathbf{H}_n)\delta\mathbf{d}, \delta\boldsymbol{\kappa}_2 = \left(\mathbf{L}_1\mathbf{H}_2 + \mathbf{L}_2\overline{\mathbf{H}}_n\right)\delta\mathbf{d}, \delta\boldsymbol{\kappa}_3 = \mathbf{H}_3\delta\mathbf{d}, \delta\boldsymbol{\kappa}_4 = \mathbf{H}_4\delta\mathbf{d}. \tag{23}$$

It is crucial to notice that it is the combination of the strain gradient terms and the classical terms of the variational formulation (21) that is responsible for capturing the size effect and the microarchitecture-dependent response, in general. These terms, respectively, include the non-classical material tensors $\mathcal{A}_i$ (specific to the microarchitecture and obtained by a generalized homogenization procedure [7]) and the classical material parameters of transversal isotropy $\mathcal{C}_i$ (obtained by a classical homogenization procedure [7]). As already noticed in the previous subsection, first, the strain gradients $\boldsymbol{\kappa}_1$ and $\boldsymbol{\kappa}_2$ and some of the components of $\boldsymbol{\kappa}_3$ and $\boldsymbol{\kappa}_4$ are composed of second-order displacement and rotation derivatives, which leads to the requirement of C^1-continuous finite elements (or to non-conforming elements). Second, some components of the strain gradients $\boldsymbol{\kappa}_3$ and $\boldsymbol{\kappa}_4$ are composed of the first-

order derivatives of rotation components analogously to the ones of strain $\boldsymbol{\varepsilon}_1$. Accordingly, the classical bending energy of the plate related to the rotations of $\boldsymbol{\varepsilon}_1$, gets augmented by the analogous strain gradient contributions. However, since the components of $\boldsymbol{\varepsilon}_1$ have z as a multiplier the corresponding bending rigidities are of the classical form "integral of $\mathcal{C}_1 z^2$ across the thickness", finally proportional to $\mathcal{C}_1 h^3$ with thickness h, whereas the bending rigidities of the corresponding components of gradients $\boldsymbol{\kappa}_3$ and $\boldsymbol{\kappa}_4$ are of the form "integral of $\mathcal{A}_{\mathrm{m}}$ across the thickness", finally proportional to $\mathcal{A}_{\mathrm{m}} h$. This leads to a crucial stiffening effect for the small values of thickness h. For linear plates [22,7], and beams especially [59,70], this feature of strain gradient (and some other) models is easy to demonstrate explicitly.

By introducing $\mathbf{f}$ as the vector of surface forces and by neglecting the body forces, the work done by the external forces is given as

$$\delta W = \int_A \delta \mathbf{d}^{\mathrm{T}} \mathbf{f} dA \tag{24}$$

In what follows, the detailed finite element formulation is provided by following the proposed energy functional for the nonlinear FSDT within the SGT.

3. Finite element method

3.1. Finite element formulation

As the first step in the FE discretization procedure, the vector of displacement components are approximated within the elements by the use of appropriate shape functions as follows:

$$\mathbf{d} = \begin{bmatrix} w_x \\ w_y \\ w_z \\ \theta_x \\ \theta_y \end{bmatrix} = \mathbb{N}\mathbb{d} \tag{25}$$

$$\mathbb{N} = \begin{bmatrix} \mathcal{N}_1 & 0 & 0 & 0 & 0 & \mathcal{N}_n & 0 & 0 & 0 & 0 \\ 0 & \mathcal{N}_1 & 0 & 0 & 0 & 0 & \mathcal{N}_n & 0 & 0 & 0 \\ 0 & 0 & \mathcal{N}_1 & 0 & 0 & \cdots & 0 & 0 & \mathcal{N}_n & 0 \\ 0 & 0 & 0 & \mathcal{N}_1 & 0 & 0 & 0 & 0 & \mathcal{N}_n & 0 \\ 0 & 0 & 0 & 0 & \mathcal{N}_1 & 0 & 0 & 0 & 0 & \mathcal{N}_n \end{bmatrix} = \begin{bmatrix} \mathbf{N}_e \otimes \mathbf{e}_1 \\ \mathbf{N}_e \otimes \mathbf{e}_2 \\ \mathbf{N}_e \otimes \mathbf{e}_3 \\ \mathbf{N}_e \otimes \mathbf{e}_4 \\ \mathbf{N}_e \otimes \mathbf{e}_5 \end{bmatrix} \tag{26}$$

in which $\mathbf{N}_e = [\mathcal{N}_1 \mathcal{N}_2 \cdots \mathcal{N}_n]$ is the vector of shape functions for each displacement component, $\mathcal{N}_i (i = 1, 2, \cdots, n)$ are the shape functions, n stands for the number of degrees of freedom (DOFs) per element for each displacement component and $\mathbf{e}_m = [\,\delta_{m1} \;\; \delta_{m2} \;\; \delta_{m3} \;\; \delta_{m4} \;\; \delta_{m5}\,]$ where $\delta_{mi} (i = 1, 2, \cdots, 5)$ is the Kronecker delta. Also, $\mathbb{d}$ is the vector of unknowns. Next, by substituting the approximation of displacement vector into strain and strain gradient vectors, one can write

$$\boldsymbol{\varepsilon}_1 = \left(\mathbf{L}_1 \mathcal{E}_1 + \frac{1}{2} \mathcal{E}_n \right) \mathbb{d}, \boldsymbol{\varepsilon}_2 = \mathcal{E}_2 \mathbb{d}, \tag{27}$$

$$\boldsymbol{\kappa}_1 = \left(\mathbf{L}_1 \mathcal{H}_1 + \frac{1}{2} \mathbf{L}_2 \mathcal{H}_n \right) \mathbb{d}, \boldsymbol{\kappa}_2 = \left(\mathbf{L}_1 \mathcal{H}_2 + \frac{1}{2} \mathbf{L}_2 \overline{\mathcal{H}}_n \right) \mathbb{d}, \boldsymbol{\kappa}_3 = \mathcal{H}_3 \mathbb{d}, \boldsymbol{\kappa}_4 = \mathcal{H}_4 \mathbb{d}, \tag{28}$$

with the following matrices:

$$\mathcal{E}_i = \mathbf{E}_i \mathbb{N} (i = 1, 2), \mathcal{E}_n = \langle \mathcal{G}_1 \mathbb{d} \rangle \mathcal{G}_2 + \langle \mathcal{G}_2 \mathbb{d} \rangle \mathcal{G}_1, \mathcal{G}_i = \mathbf{G}_i \mathbb{N} (i = 1, 2), \tag{29}$$

$$\begin{aligned} \mathcal{H}_i &= \mathbf{H}_i \mathbb{N} (i = 1, 2, 3, 4), \mathcal{H}_n = \langle \mathcal{Q}_1 \mathbb{d} \rangle \mathcal{Q}_2 + \langle \mathcal{Q}_2 \mathbb{d} \rangle \mathcal{Q}_1, \overline{\mathcal{H}}_n \\ &= \langle \mathcal{Q}_3 \mathbb{d} \rangle \mathcal{Q}_4 + \langle \mathcal{Q}_4 \mathbb{d} \rangle \mathcal{Q}_3, \mathcal{Q}_i = \mathbf{Q}_i \mathbb{N} (i = 1, 2, 3, 4) \end{aligned} \tag{30}$$

Finally, by substituting Eqs. (25), (27) and (28) into (21) and (24), and integration through the thickness direction, the discretized FE version of the energy functional is represented as

$$\begin{aligned} &\int_A \delta \mathbb{d}^{\mathrm{T}} \Big(\mathcal{E}_1^{\mathrm{T}} \mathcal{C}_1^* \mathcal{E}_1 + \mathcal{E}_2^{\mathrm{T}} \mathcal{C}_2^* \mathcal{E}_2 + \frac{1}{2} \mathcal{E}_1^{\mathrm{T}} \mathcal{C}_3^* \mathcal{E}_n + \mathcal{E}_n^{\mathrm{T}} \mathcal{C}_4^* \mathcal{E}_1 + \frac{1}{2} \mathcal{E}_n^{\mathrm{T}} \mathcal{C}_5^* \mathcal{E}_n + \sum_{m=1}^{4} \mathcal{H}_{\mathrm{m}}^{\mathrm{T}} \mathcal{A}_{\mathrm{m}}^* \mathcal{H}_{\mathrm{m}} \\ &+ \frac{1}{2} \mathcal{H}_1^{\mathrm{T}} \mathcal{A}_5^* \mathcal{H}_n + \frac{1}{2} \mathcal{H}_2^{\mathrm{T}} \mathcal{A}_6^* \overline{\mathcal{H}}_n + \mathcal{H}_n^{\mathrm{T}} \mathcal{A}_7^* \mathcal{H}_1 + \overline{\mathbf{H}}_n^{\mathrm{T}} \mathcal{A}_8^* \mathcal{H}_2 + \frac{1}{2} \mathcal{H}_n^{\mathrm{T}} \mathcal{A}_9^* \mathcal{H}_n \\ &+ \frac{1}{2} \overline{\mathcal{H}}_n^{\mathrm{T}} \mathcal{A}_{10}^* \overline{\mathcal{H}}_n \Big) \mathbb{d} dA + \int_A \delta \mathbb{d}^{\mathrm{T}} \mathbb{N}^{\mathrm{T}} \mathbf{f} dA \\ &= 0 \end{aligned} \tag{31}$$

in which the following classical and higher-order material matrices are considered:

$$\begin{aligned} &\mathcal{C}_1^* = \int_{-h/2}^{h/2} \mathbf{L}_1^{\mathrm{T}} \mathcal{C}_1 \mathbf{L}_1 dz, \mathcal{C}_2^* = k_s \int_{-h/2}^{h/2} \mathcal{C}_2 dz, \mathcal{C}_3^* = \int_{-h/2}^{h/2} \mathbf{L}_1^{\mathrm{T}} \mathcal{C}_1 dz = \mathcal{C}_4^{*\mathrm{T}}, \mathcal{C}_5^* = \int_{-h/2}^{h/2} \mathcal{C}_1 dz \\ &\mathcal{A}_1^* = \int_{-h/2}^{h/2} \mathbf{L}_1^{\mathrm{T}} \mathcal{A}_1 \mathbf{L}_1 dz, \mathcal{A}_2^* = \int_{-h/2}^{h/2} \mathbf{L}_1^{\mathrm{T}} \mathcal{A}_2 \mathbf{L}_1 dz, \mathcal{A}_3^* = \int_{-h/2}^{h/2} \mathcal{A}_3 dz \\ &\mathcal{A}_4^* = \int_{-h/2}^{h/2} \mathcal{A}_4 dz, \mathcal{A}_5^* = \int_{-h/2}^{h/2} \mathbf{L}_1^{\mathrm{T}} \mathcal{A}_1 \mathbf{L}_2 dz = \mathcal{A}_7^{*\mathrm{T}}, \mathcal{A}_6^* = \int_{-h/2}^{h/2} \mathbf{L}_1^{\mathrm{T}} \mathcal{A}_2 \mathbf{L}_2 dz = \mathcal{A}_8^{*\mathrm{T}} \mathcal{A}_9^* \\ &= \int_{-h/2}^{h/2} \mathbf{L}_2^{\mathrm{T}} \mathcal{A}_1 \mathbf{L}_2 dz, \mathcal{A}_{10}^* = \int_{-h/2}^{h/2} \mathbf{L}_2^{\mathrm{T}} \mathcal{A}_2 \mathbf{L}_2 dz \end{aligned} \tag{32}$$

Accordingly, the energy functional of Eq. (31) results in the following nonlinear discretized governing equations:

$$\left(\mathbf{K}_l + \frac{1}{2} \mathbf{K}_{nl} + \frac{1}{3} \mathbf{K}_{nl}^* \right) \mathbb{d} + \mathbf{F} = 0 \tag{33}$$

with the stiffness matrices

$$\begin{aligned} \mathbf{K}_l &= \int_A \left(\mathcal{E}_1^{\mathrm{T}} \mathcal{C}_1^* \mathcal{E}_1 + \mathcal{E}_2^{\mathrm{T}} \mathcal{C}_2^* \mathcal{E}_2 + \sum\nolimits_{m=1}^{4} \mathcal{H}_{\mathrm{m}}^{\mathrm{T}} \mathcal{A}_{\mathrm{m}}^* \mathcal{H}_{\mathrm{m}} \right) dA, \\ \mathbf{K}_{nl} &= \int_A \left(\mathcal{E}_1^{\mathrm{T}} \mathcal{C}_3^* \mathcal{E}_n + 2 \mathcal{E}_n^{\mathrm{T}} \mathcal{C}_4^* \mathcal{E}_1 + \mathcal{H}_1^{\mathrm{T}} \mathcal{A}_5^* \mathcal{H}_n + \mathcal{H}_2^{\mathrm{T}} \mathcal{A}_6^* \overline{\mathcal{H}}_n + 2 \mathcal{H}_n^{\mathrm{T}} \mathcal{A}_7^* \mathcal{H}_1 + 2 \overline{\mathbf{H}}_n^{\mathrm{T}} \mathcal{A}_8^* \mathcal{H}_2 \right) dA, \\ \mathbf{K}_{nl}^* &= \frac{3}{2} \int_A \left(\mathcal{E}_n^{\mathrm{T}} \mathcal{C}_5^* \mathcal{E}_n + \mathcal{H}_n^{\mathrm{T}} \mathcal{A}_9^* \mathcal{H}_n + \overline{\mathbf{H}}_n^{\mathrm{T}} \mathcal{A}_{10}^* \overline{\mathcal{H}}_n \right) dA \end{aligned} \tag{34}$$

in which subscripts l and nl denote the linear and nonlinear parts, respectively, whereas superscript * stands for the purely nonlinear terms. The force vector is also defined as

$$\mathbf{F} = \int_A \mathbb{N}^{\mathrm{T}} \mathbf{f} dA \tag{35}$$

The linear part $\mathbf{K}_l$ of the stiffness matrix, defined in Eq. (34), includes strain gradient components (the sum from 1 to 4 in the integrand of $\mathbf{K}_l$) which are either of higher-order or of the same order as the components of the classical terms (the first two terms in the integrand of $\mathbf{K}_l$). These different non-classical terms can be traced from (30) and (28) via (20) back to the strain gradients defined in Eqs. (9)–(11) and then compared to their classical counterparts (forming the first two terms of $\mathbf{K}_l$) which, in turn, can be traced from (29) and (27) via (20) back to (5). Analogous pairs appear in the nonlinear parts of the stiffness matrix (coupling the in-plane and transversal deformations) but tracing them is more cumbersome.

Finally, it should be noticed that the non-standard finite element method introduced next, in turn, aims at being loyal to the governing variational formulation although it is not conforming but only quasi-conforming.

3.2. Quasi-C^1-continuous six-node triangular element

The FE formulation for the nonlinear strain gradient FSDT was formulated in the previous subsection. As can be seen, the strain energy functional is presented by using the first- and second-order derivatives of the displacement field. Owing to the presence of the second-order derivatives, the standard C^0-continuous Lagrangian elements cannot be utilized to approximate the field variables. Hence, a quasi-C^1-continuous six-node triangular element is introduced herein to perform a quasi-conforming FE discretization and, accordingly, an accurate FE analysis. The element formulation is derived in terms of a local area coordinate (LAC) system (L_1, L_2, L_3). As shown in Fig. 3, to respond to the higher-order continuity requirements, the first-order derivatives of the field variable are also exhibited as the nodal values, in addition to the classical field variable values.

By introducing ψ as a sample scalar field, Ψ_i as the values of the scalar field at nodes and Ψ_i^x, Ψ_i^y as the values of the first-order derivatives of the scalar field, one can write the following relations:

$$\psi(\mathbf{L}_i) = \Psi_i, \frac{\partial \psi}{\partial x}\Big|\mathbf{L} = \mathbf{L}_i = \Psi_i^x, \frac{\partial \psi}{\partial y}\Big|\mathbf{L} = \mathbf{L}_i = \Psi_i^y, (i = 1,2,3,4,5,6) \tag{36}$$

in which $\mathbf{L} = [L_1 L_2 L_3]$ is the vector of the LACs and $\mathbf{L}_i = [L_1^i L_2^i L_3^i]$ denotes the vector of the LACs at node i which can be found in Table 1.

Table 1
The local area coordinates of the six-node triangular plate element.

	$\mathbf{L}_i = [L_1^i L_2^i L_3^i]$
Node 1 ($i = 1$)	[1 0 0]
Node 2 ($i = 2$)	[0 1 0]
Node 3 ($i = 3$)	[0 0 1]
Node 4 ($i = 4$)	[1/2 1/2 0]
Node 5 ($i = 5$)	[0 1/2 1/2]
Node 6 ($i = 6$)	[1/2 0 1/2]

Since the 6-node triangular element has been considered and each node has three nodal values (for each variable) including the field variable (Ψ_i) and its first-order derivatives (Ψ_i^x,Ψ_i^y), it is figured out that the proposed triangular element has 18 DOFs for each scalar field. As an element with higher-order polynomial basis functions, this element is not considered to be prone to the so-called numerical locking known be a critical issue for low-order beam, plate and shell elements of the FSDT (cf. [58,83]).

Now, by introducing the row vector $\mathbf{\Gamma}(\mathbf{L})_{1\times 18}$ as the vector of basis functions in the form

$$\mathbf{\Gamma}(\mathbf{L}) = \left[L_1 L_2 L_3 L_1 L_2 L_2 L_3 L_1 L_3 L_1^2 L_2 L_2^2 L_3 L_3^2 L_1 L_1^2 L_2^2 L_2^2 L_3^2 L_3^2 L_1^2 L_1^3 L_2 L_2^3 L_3 L_3^3 L_1 L_1^4 L_2 L_2^4 L_3 L_3^4 L_1\right], \tag{37}$$

and the column vector $\mathbf{C}_{18\times 1}$ of unknowns as

$$\mathbf{C} = [c_1 \quad c_2 \quad \cdots \quad c_{18}]^{\mathrm{T}}, \tag{38}$$

the approximation of the scalar field within the element is

$$\psi(\mathbf{L}) = \mathbf{\Gamma}(\mathbf{L})\mathbf{C}. \tag{39}$$

Then, substituting Eq. (39) into (36) results in the set of algebraic equations for the unknown vector $\mathbf{C}$ as

$$\mathbf{\Psi} = V\mathbf{C}, \tag{40}$$

with

$$\mathbf{\Psi} = \left[\Psi_1 \quad \Psi_1^x \quad \Psi_1^y \quad \Psi_2 \quad \Psi_2^x \quad \Psi_2^y \quad \cdots \quad \Psi_6 \quad \Psi_6^x \quad \Psi_6^y\right]^{\mathrm{T}}, \tag{41}$$

$$\mathfrak{V} = \begin{bmatrix} \mathbf{\Gamma}^*(\mathbf{L}_1) \\ \mathbf{\Gamma}^*(\mathbf{L}_2) \\ \vdots \\ \mathbf{\Gamma}^*(\mathbf{L}_6) \end{bmatrix}_{18\times 18}, \quad \mathbf{\Gamma}^*(\mathbf{L}_i) = \begin{bmatrix} \mathbf{\Gamma}(\mathbf{L}_i) \\ \dfrac{\partial \mathbf{\Gamma}(\mathbf{L})}{\partial x}\Big|\mathbf{L} = \mathbf{L}_i \\ \dfrac{\partial \mathbf{\Gamma}(\mathbf{L})}{\partial y}\Big|\mathbf{L} = \mathbf{L}_i \end{bmatrix}_{3\times 18} \tag{42}$$

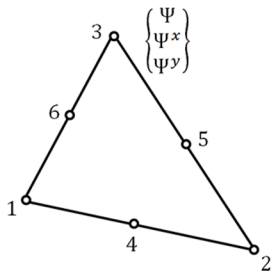

- 6 nodes (o); 5 field variables (three displacements and two rotations)
- 3 DOFs per node for each field variable (the variable itself and its partial derivatives denoted with superscripts x and y)
- 18 DOFs per element for each field variable
- 90 DOFs per element in total

Fig. 3. Description of the higher-order 6-node triangular plate element.

which can be solved as $\mathbf{C} = V^{-1}\mathbf{\Psi}$. Substituting this into Eq. (39) leads to the following relation:

$$\psi(\mathbf{L}) = \mathbf{\Gamma}(\mathbf{L})\mathfrak{R}^{-1}\mathbf{\Psi} = \mathbf{N}_e\mathbf{\Psi}, \tag{43}$$

where

$$\mathbf{N}_e = \mathbf{\Gamma}(\mathbf{L})V^{-1} \tag{44}$$

is the vector of shape functions for the proposed triangular element used in Eq. (26). The details of how to differentiate the vector of basis functions with respect to the global coordinates (x,y) can be found in [55].

4. Numerical results and discussions

In the previous section, by introducing the quasi-C^1-continuous six-node triangular element, the FE governing equations of the nonlinear bending analysis were derived based on the nonlinear strain gradient FSDT of plates. The stiffness matrices and force vector can be calculated via the numerical Gauss quadrature integration technique through Eqs. (34) and (35). The total governing equations can be obtained by using an appropriate assembly procedure. Finally, the Newton-Raphson iteration technique is employed to find the nonlinear bending response.

As explained, in this study the nonlinear bending analysis of cellular plates is presented by following the nonlinear plate model of the SGT. Indeed, the transversally isotropic 3D cellular plates having equitriangularly prismatic cores are modeled by using the size-dependent plate theory in which the classical and higher-order material properties are determined through a numerical homogenization technique by comparing the results of the (reference) 3D full-field and the (proposed) 2D plate models. In the present study, cellular plates made of steel are considered as shown in Fig. 4 with the geometrical parameters presented in Table 2. The number of the layers and related geometrical parameters of the plate such as the length-to-thickness ratio and the aspect ratio are presented for all numerical results. Based on the number of layers and the thickness of each layer (i.e. $a_3/2 = 4.33$ based on Table 2), the total thickness of the plate (h) can be obtained. Then, namely for rectangular plates, the length-to-thickness ratio (a/h) is used to determine the length of the plate and the aspect ratio (a/b) can be also used to give the width of the plate. The results corresponding to the 3D full-field model are

Table 2
The geometrical parameters of the triangular unit cell of Fig. 3.

a_1(mm)	a_2(mm)	a_3(mm)	a_4(mm)	$\alpha b0$
5	5	8.66	0.5	60

Table 3
The classical effective constitutive parameters for transversally isotropic classical elasticity (GPa) [7].

$\mathscr{C}_{11}$	$\mathscr{C}_{12}$	$\mathscr{C}_{22}$	$\mathscr{C}_{44}$	$\mathscr{C}_{55}$	$\mathscr{C}_{66}$
26.27	6.57	64.96	14.43	9.76	14.43

Table 4
The non-classical constitutive parameters for the SG plate model (kN) [7].

$c^1_{11} = c^2_{22} = c^3_{11}$	63.96
$c^1_{12} = c^2_{12} = c^3_{13}$	17.59
$c^1_{22} = c^2_{11} = c^3_{33}$	50.30
$c^1_{33} = c^2_{33} = c^4_{11}$	17.78
$c^3_{22} = c^4_{33}$	12.02
$c^3_{44} = c^4_{22}$	17.78
$c^1_{13} = c^1_{23} = c^2_{13} = c^2_{23} = c^3_{12} = c^3_{14} = c^3_{23} = c^3_{24} = c^3_{34} = c^4_{12} = c^4_{13} = c^4_{23} =$	0

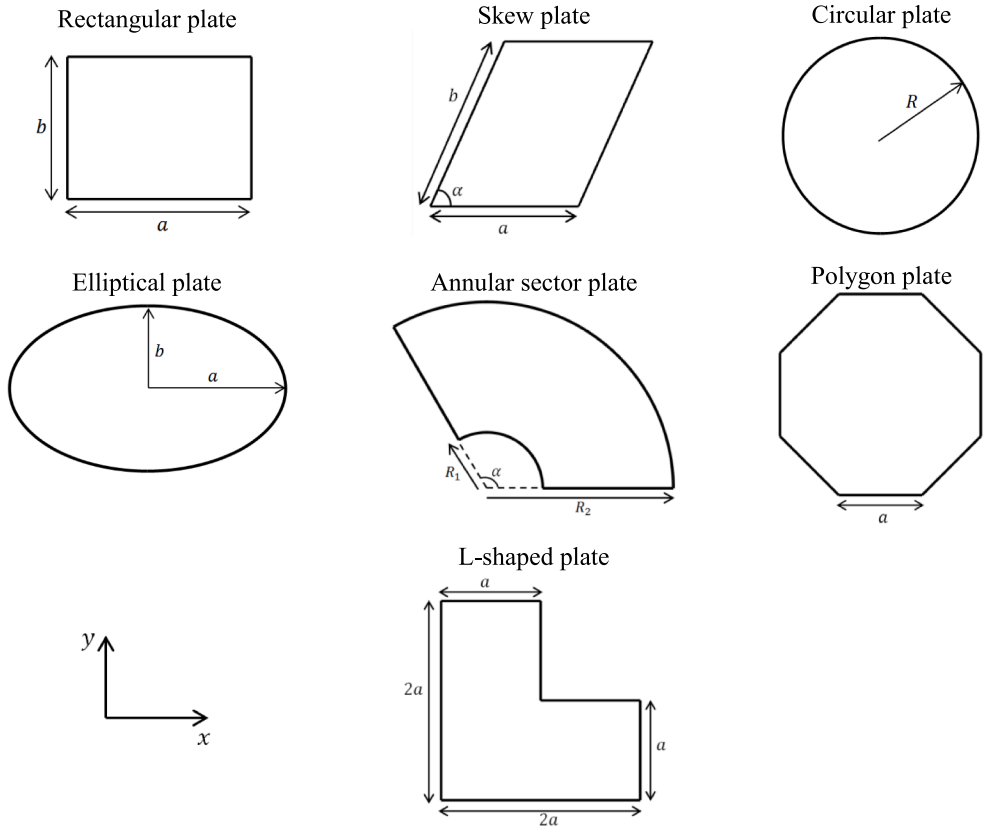

Fig. 4. Schematic views and geometrical parameters for different plate domains.

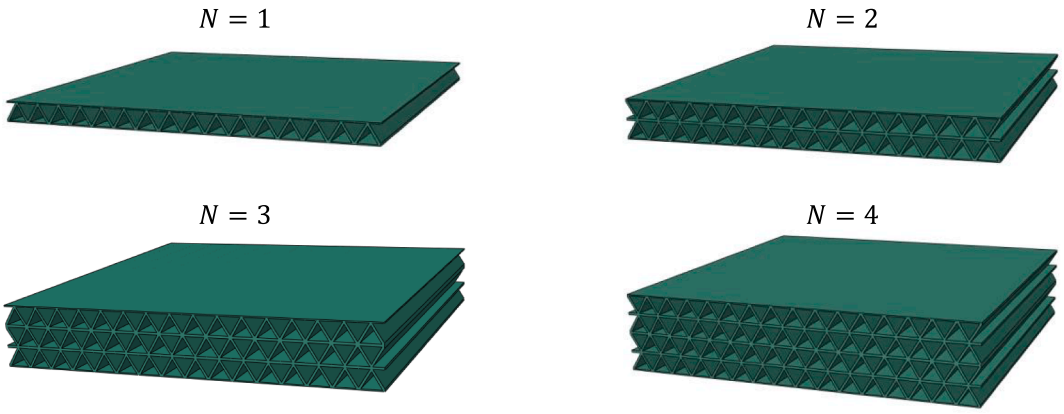

Fig. 5. Representations of rectangular cellular plates with different numbers (N) of layers.

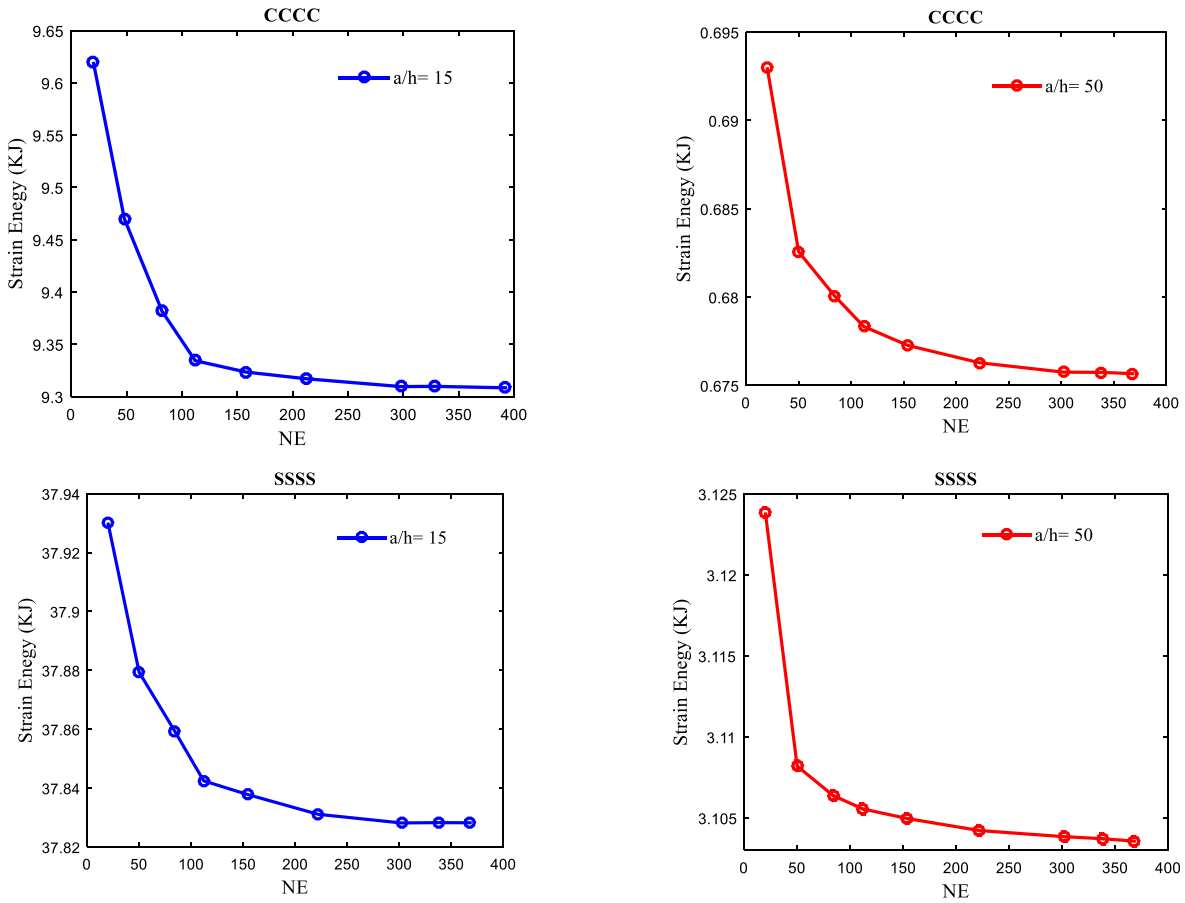

Fig. 6. Convergence studies with respect to the total strain energy of the strain gradient FSDT plate model cellular square plates (corresponding to the single-layer case $N = 1$) with different length-to-thickness ratios a/h (loading $Q = 500$).

based on using 10-node tetrahedral elements of type C3D10 of the commercial Abaqus FE software. The classical and strain gradient constitutive parameters for this kind of cellular structure are presented in Tables 3 and 4 according to the work of Kakalo and Niiranen [7]. It should be noted that constitutively reduced strain gradient plate models (of both the Kirchhoff and FSDT types) were considered in [7], whereas a full SGT plate model is employed in this study to accurately present the geometrically nonlinear analysis coupling the bending and membrane terms of deformation.

The numerical results for the nonlinear bending analysis of cellular structures are presented for different shapes of plate mid-surfaces: rectangular, skew, circular, elliptical, annularly sectorial, polygonal and L-shaped. The schematic view and the corresponding geometrical parameters can be found in Fig. 4. In order to investigate the size effect in cellular structures, plates with different numbers (N) of micro-architectural layers are considered: plates with one, two, three and four layers are depicted as examples in Fig. 5. Clamped (C), simply supported (S) and free (F) boundaries are considered with the following constraints:

$$\begin{aligned} &\text{clamped} : \mathscr{u}_n = \mathscr{u}_s = \mathscr{u}_z = \Theta_n = \Theta_s = 0, \\ &\text{simply supported} : \begin{cases} \text{immovable} : \mathscr{u}_n = \mathscr{u}_s = \mathscr{u}_z = \Theta_s = 0, \\ \text{movable} : \mathscr{u}_s = \mathscr{u}_z = \Theta_s = 0, \end{cases} \end{aligned} \tag{45}$$

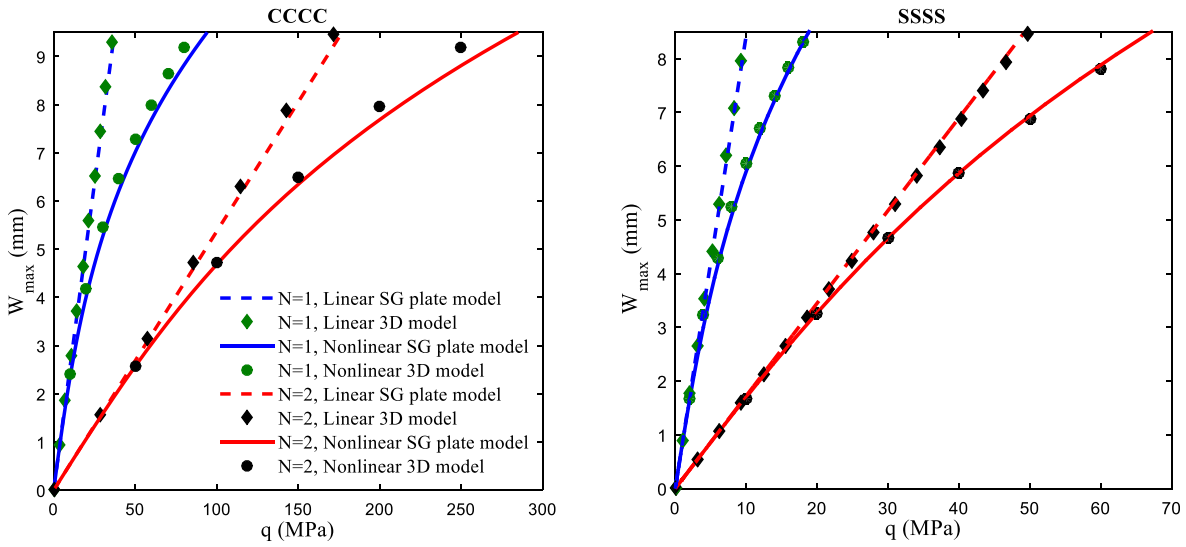

Fig. 7. A comparison of the (proposed) strain gradient FSDT and (the reference) 3D models of classical elasticity with respect to the maximum deflection for linear and nonlinear bending of one- and two-layer cellular square plates ($a = b = 100$mm).

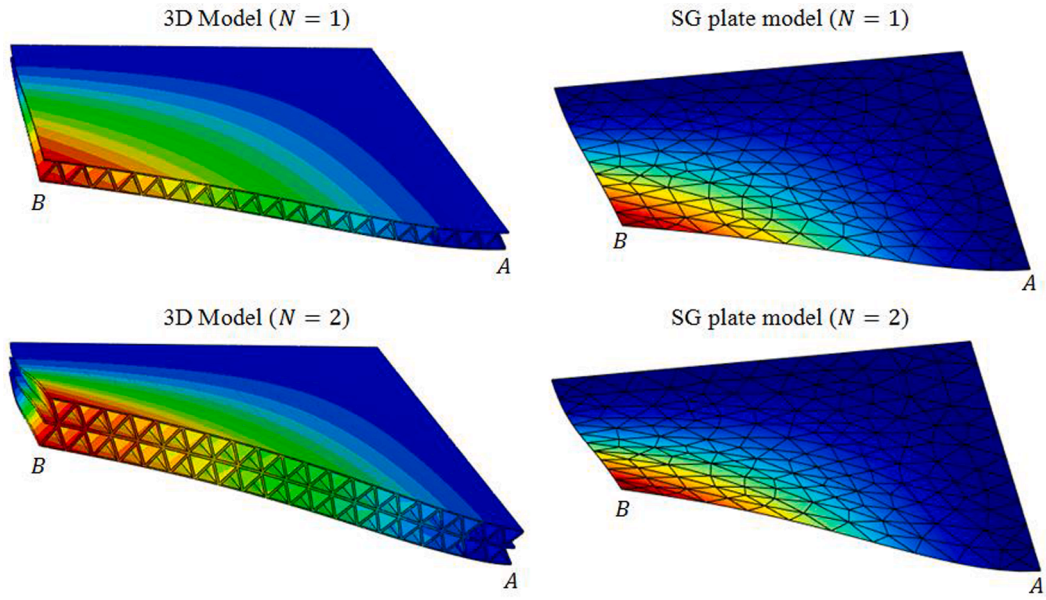

Fig. 8. A comparison of the normalized distribution of the transverse displacement of one- and two-layer rectangular cellular plates based on (the reference) 3D models of classical elasticity (left) and the (proposed) strain gradient FSDT (right) with the FCFC boundary condition ($a = b = 100$).

with $\mathcal{M}_n = c_x\mathcal{M}_x + c_y\mathcal{M}_y, \mathcal{M}_s = -c_y\mathcal{M}_x + c_x\mathcal{M}_y, \Theta_n = c_x\theta_x + c_y\theta_y$ and $\Theta_s = -c_y\theta_x + c_x\theta_y$ in which c_x and c_y denote the components of the outward unit normal vector of the boundary curve. If not otherwise stated, the movable simply supported boundary condition is used.

As the first result, a convergence study of the total strain energy in a nonlinear bending problem is demonstrated in Fig. 6 for square plates (corresponding to the single-layer plate indicated by $N = 1$ in Fig. 5) with fully clamped (CCCC) and fully simply supported (SSSS) edges with two length-to-thickness ratios, i.e., $a/h = 15, 50$. It is obviously shown that increasing the number of elements (NE) leads to fairly quick convergence (with strain energy as a measure) for both boundary conditions types and for both aspect ratios.

Next, in order to compare the (proposed) strain gradient plate theory and the (reference) 3D full-field model, the linear and nonlinear bending responses for the same (CCCC and SSSS) plates are demonstrated in Fig. 7 (with the maximum deflection as a measure).

As another set of comparison studies, the normalized distributions of the transverse displacement of one- and two-layer rectangular plates obtained with the 3D model and the strain gradient plate model are compared in Fig. 8. To give more details, the non-dimensional deflection of square and skew ($\alpha = 30$) plates along the bottom edge (path AB as shown in Fig. 8) are illustrated in Fig. 9. Although small deviations from the reference curves can be seen for the CCCC plate, the overall agreement of the results in Figs. 7–9 demonstrates the accuracy of the SG plate model up to the non-linear regime.

For demonstrating the size-effect related to the microarchitecture, described in the Introduction with Figs. 1 and 2, the bending response for a series of plates with different numbers of layers (for $N = 1, 2, \ldots, 8$) is analyzed within the geometrically nonlinear regime. For highlighting the impacts of the microarchitecture and the number of layers, and for emphasizing the importance of the strain gradient theory, the bending rigidity – now defined as $qa^2/W_{max}t$ for a fully clamped and uniformly loaded square plate (with load level q and side length a) – is presented in Fig. 10 for both strain gradient and classical FSDT plates and with both

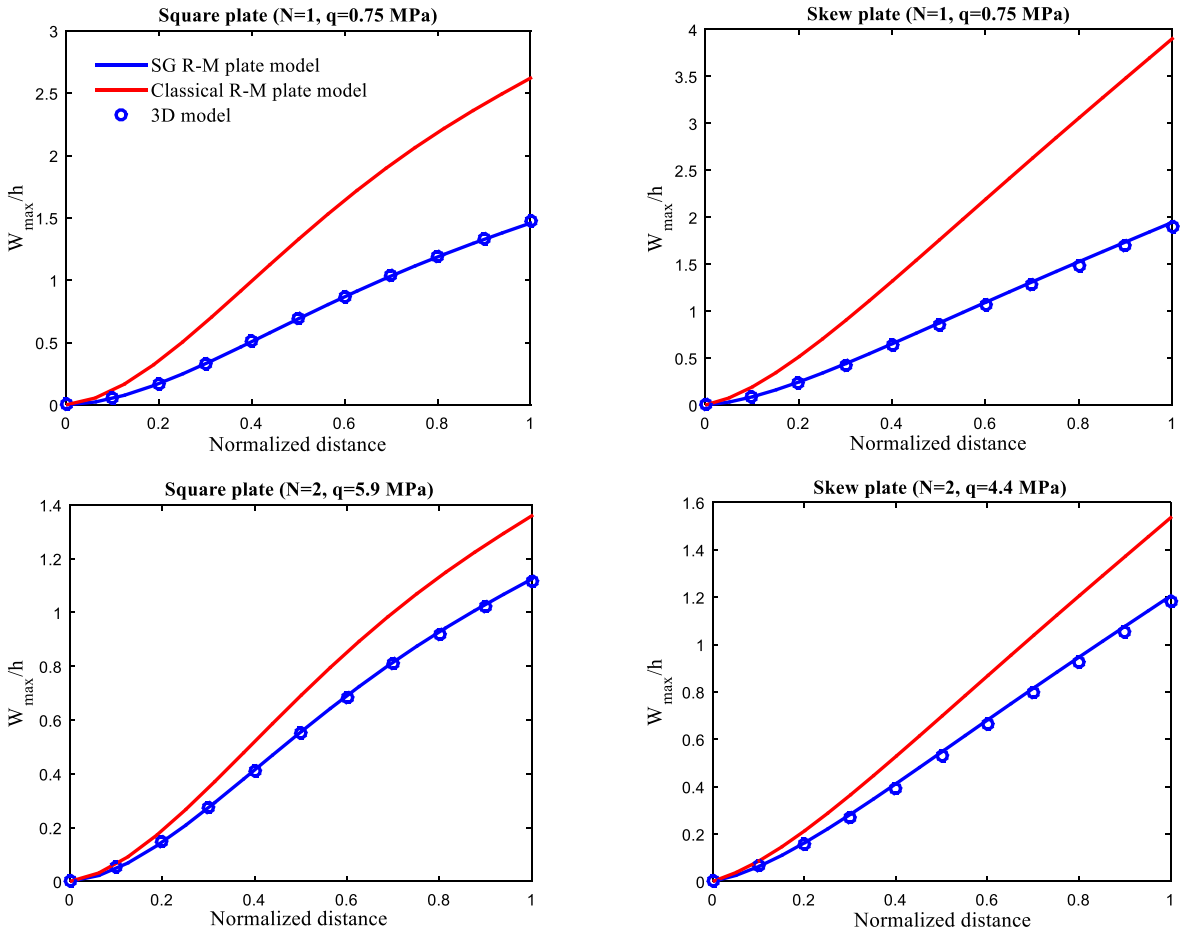

Fig. 9. Model validation for the non-dimensional deflection of one- and two-layer cellular square and skew ($\alpha = 30$) plates along the bottom edge (path *AB* as shown in Fig. 7) for the FCFC boundary condition ($a = b = 100$mm).

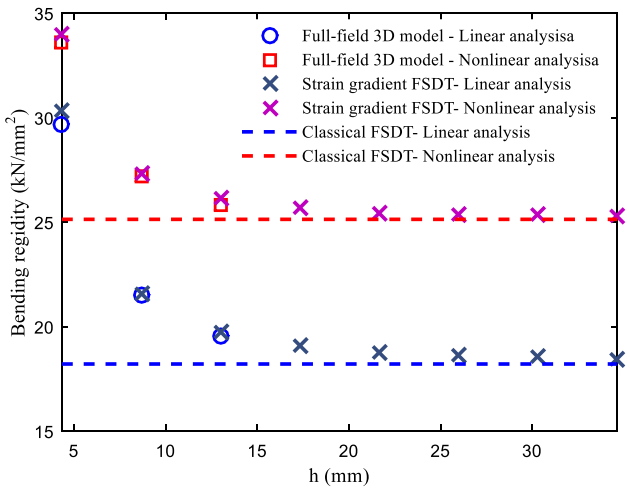

Fig. 10. Bending rigidities of clamped cellular square plates ($a/h = 11.55, q = 1500$MPa).

geometrically linear and nonlinear analysis. For comparison, the numerical results of the corresponding 3D full-field models are also included for $N = 1, 2, 3$ (circles and squares). As can be seen, the results based on the 2D strain gradient plate model are fairly consistent with the results of the 3D model, whereas the classical FSDT cannot capture the microarchitectured-dependent mechanical behavior.

In what follows, detailed numerical examples are presented for the nonlinear bending analysis of different plate domains, with the variation of the ratio between the non-dimensional deflection ($W_{max}/h = w_z^{max}/h$) and the non-dimensional transverse load ($Q = qa^4/C_{11}h^4$) reported as a measure of the nonlinear bending response. Fig. 11 demonstrates the nonlinear bending responses of fully clamped cellular plates of several shapes for a different number of cellular layers ($N = 1, 2, 3$) in order to highlight the impact of the number of layers considered as a size-effect – as the solutions converge towards the corresponding classical plate solutions as the number of layers increases. Accordingly, it is observed that despite the constant length-to-thickness ratio, the plates with one layer ($N = 1$) show relatively stiffer bending behavior due to the size effect captured by the SG plate model. On the other hand, one can see that the results corresponding to the three-layer ($N = 3$) plates are quite close to the corresponding results of the classical FSDT. In accordance with this observation, in [7] considering the linear regime, it was shown that with eight layers ($N = 8$) the difference between the classical and strain gradient models is very small. To further illustrate this bending analysis, deflection distributions for the different plate geometries are represented in Fig. 12.

The effect of the length-to-thickness ratio on the size-dependent nonlinear bending response of the different shapes of plates with fully clamped boundaries is investigated in Fig. 13: the nonlinear bending responses (with the maximum deflection as a measure) are presented for two different length-to-thickness ratios (thin, thick) for one- and two-layer plates ($N = 1, 2$). Comparing the results for the thin and thick plates reveals that the cellular microstructure has a more considerable size effect for the thin plates than for the thick ones. One can see, for instance, that in the case of the rectangular plate and for $Q = 400$, the

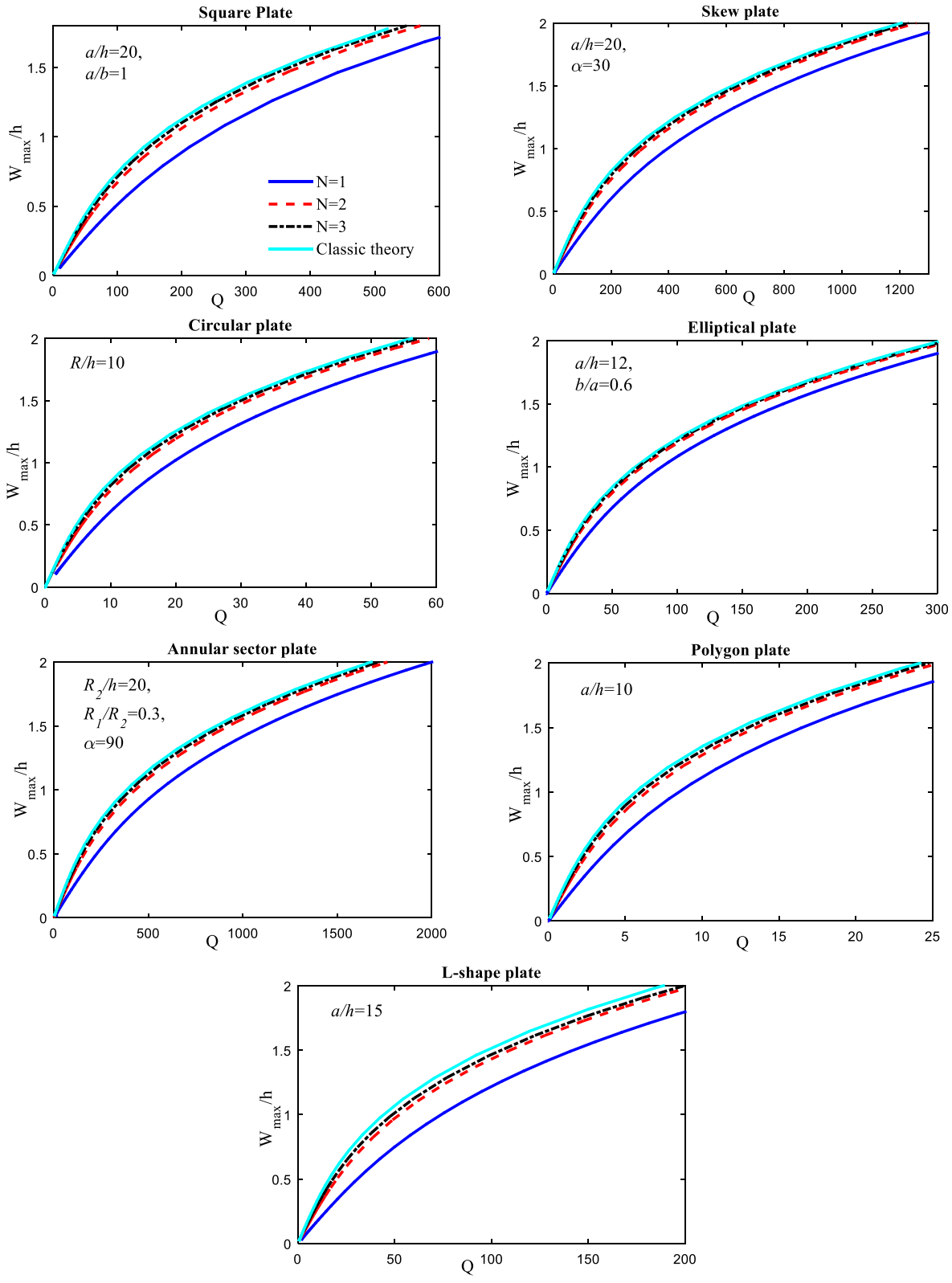

Fig. 11. The nonlinear bending responses of fully clamped cellular plates of different geometries with different number of layers.

difference in the maximum non-dimensional deflection of one- and two-layer plates is 6.7% for $a/h = 10$ (thick), while the corresponding value for $a/h = 50$ (thin) is 12.8%.

Demonstrated in Fig. 14 are the nonlinear bending responses of rectangular and skew one-layer cellular plates for different sets of boundary conditions. In the case of the skew plate, the skew angle is $\alpha =$ 30 and for both cases the length-to-thickness ratio is $a/h = 20$. The notation for the boundary conditions is the following: CCSS implies that the left and right edges are clamped and the other two edges are simply supported. As expected, the fully clamped supports lead to the stiffest structure. On the other hand, the fully simply supported SSSS plate has the most flexible bending behavior and gives even larger deflection

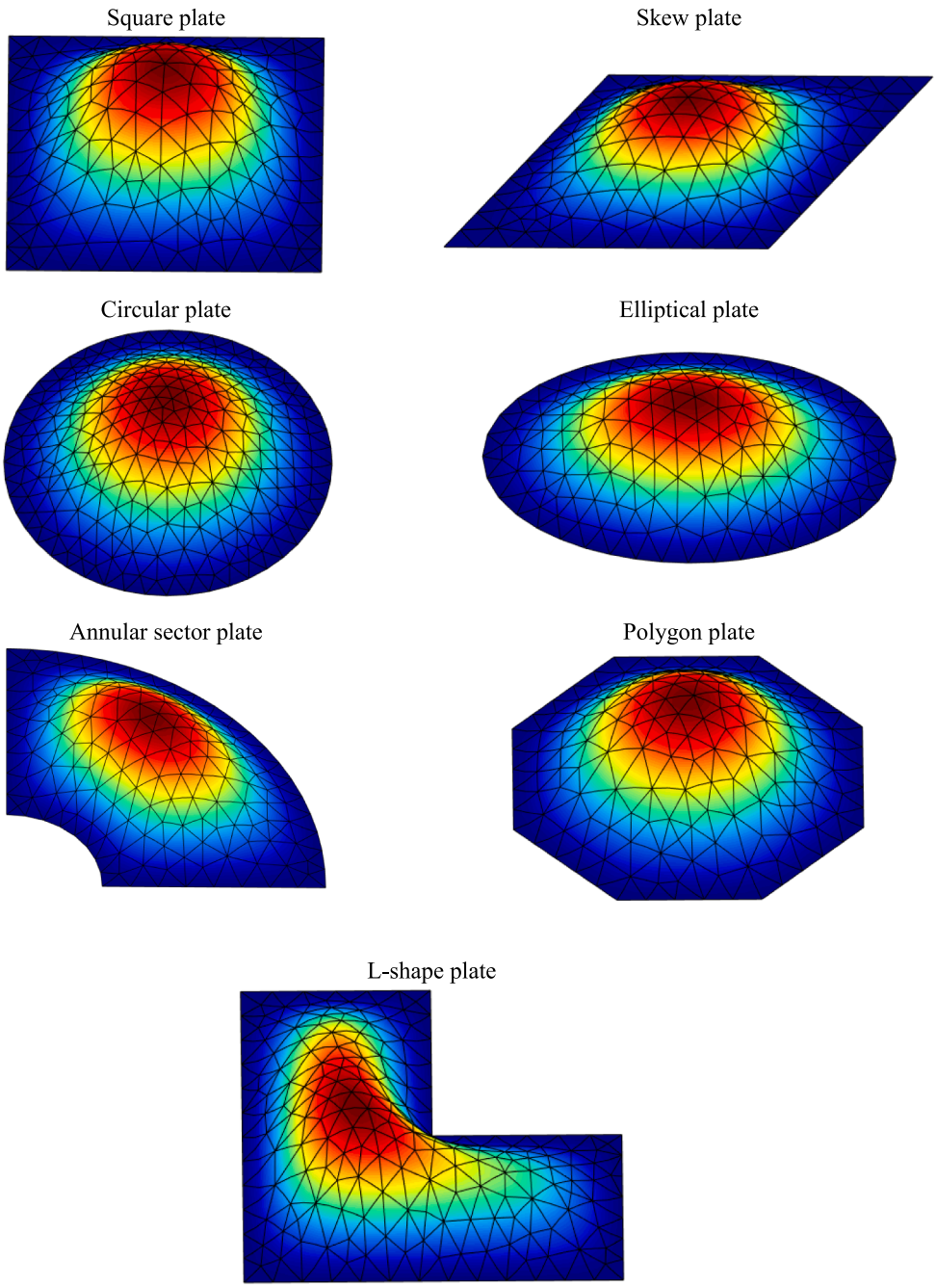

Fig. 12. Deflection distributions for cellular plates of different geometries with fully clamped boundary conditions (with the same geometrical parameters as in Fig. 9).

values than the FFCC boundary condition, whereas the results for CCSS and CSCS are quite close to each other.

The impact of the aspect ratio (a/b) on the nonlinear bending response of fully clamped one-layer square and skew ($\alpha = 30$) plates are studied in Fig. 15. Since the cellular plates are orthotropic, aspect ratios from the range of $a/b = 0.6$ to $a/b = 4$ are considered. The results indicate that increasing the a/b ratio makes the plates more flexible and decreases the influence of the terms related to the geometrical nonlinearity. Note that for larger aspect ratios, there is larger deflection, however, it can be seen that for reasonable deflection ratios, i.e., $W_{max}/h < 2$, the differences between the linear and nonlinear responses are more considerable for smaller aspect ratios.

Fig. 16 provides the nonlinear bending responses of skew plates for different skew angles with clamped and simply supported edges. As can be observed, for plates with larger skew angles the deflection values are smaller as the effect of nonlinear strains is more remarkable. Indeed, a larger skew angle makes the plate more stable and decreases the deflection.

The nonlinear bending responses of one-layer elliptical plates with clamped and immovably simply supported edges are illustrated in Fig. 17 for several aspect ratios. One can see that an increase in the aspect ratio makes the plate more flexible and increases the value of the non-dimensional deflection. On the other hand, it is concluded that elliptical plates of smaller aspect ratios are most affected by geometric nonlinearity.

The normalized distributions of the transversal displacement component for one- and two-layer annular sector plates are depicted in Fig. 18: for the (reference) 3D model (left) and for the (proposed) strain

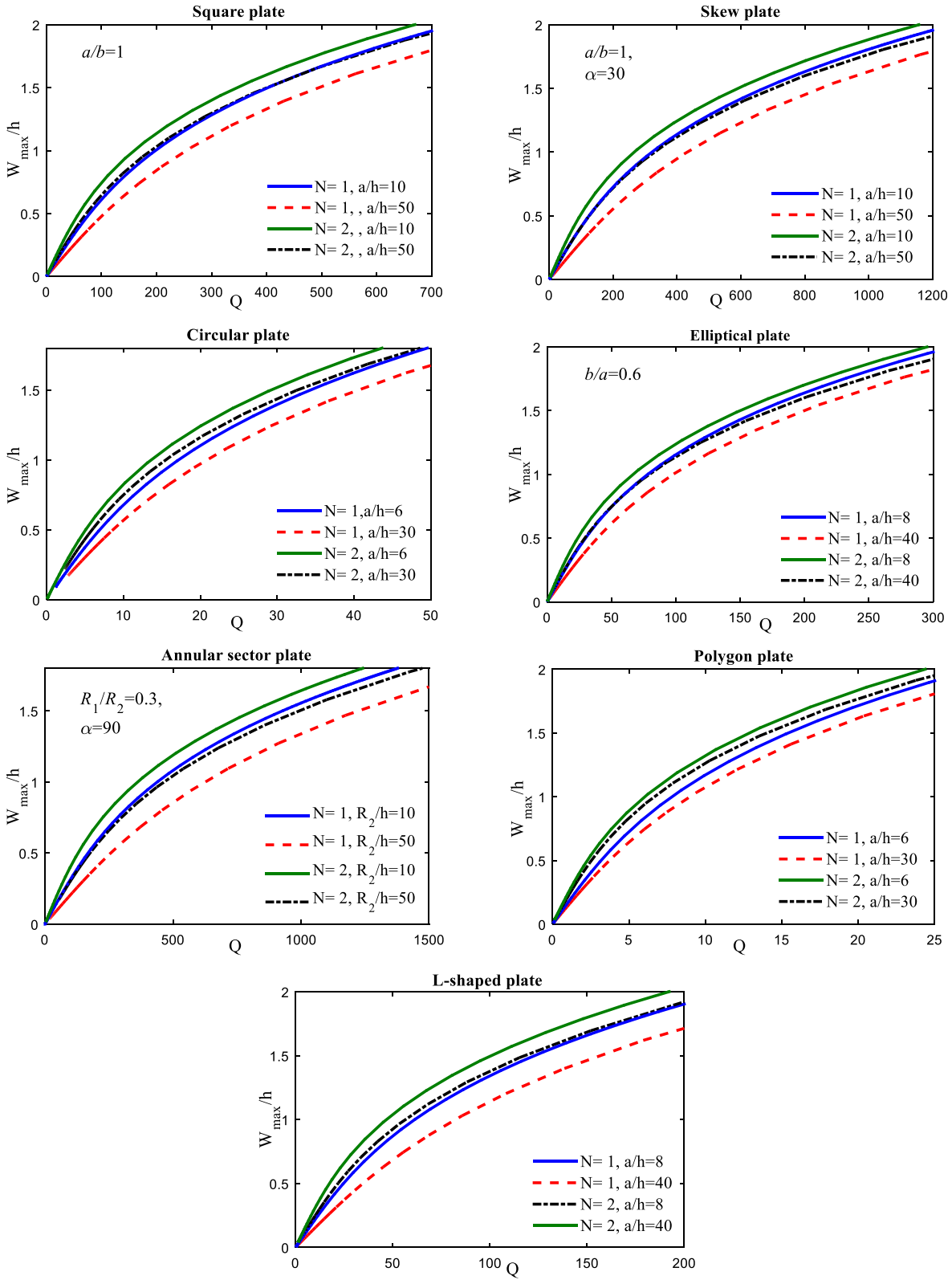

Fig. 13. The impact of the length-to-thickness ratio a/h on the nonlinear bending behavior of fully clamped cellular one- and two-layer cellular plates of different shapes.

gradient plate model (right). Besides, the distributions of the non-dimensional deflection along the longer curved edge (path AB as depicted in Fig. 18) are plotted in Fig. 19 for both models. It can be generally seen that the classical shear deformable plate model essentially underestimates the bending rigidity of cellular plates.

The effect of the sector angle (($\alpha = 90, 150, 210$) and the small-to-large ratio of the annular radii ($R_1/R_2 = 0.1, 0.3, 0.5$) on the nonlinear bending response of fully clamped one-layer annular sector plates are investigated in Fig. 20. It is found that the results for $\alpha = 90, 150$ are quite close to each other, whereas $\alpha = 210$ results in larger deflection

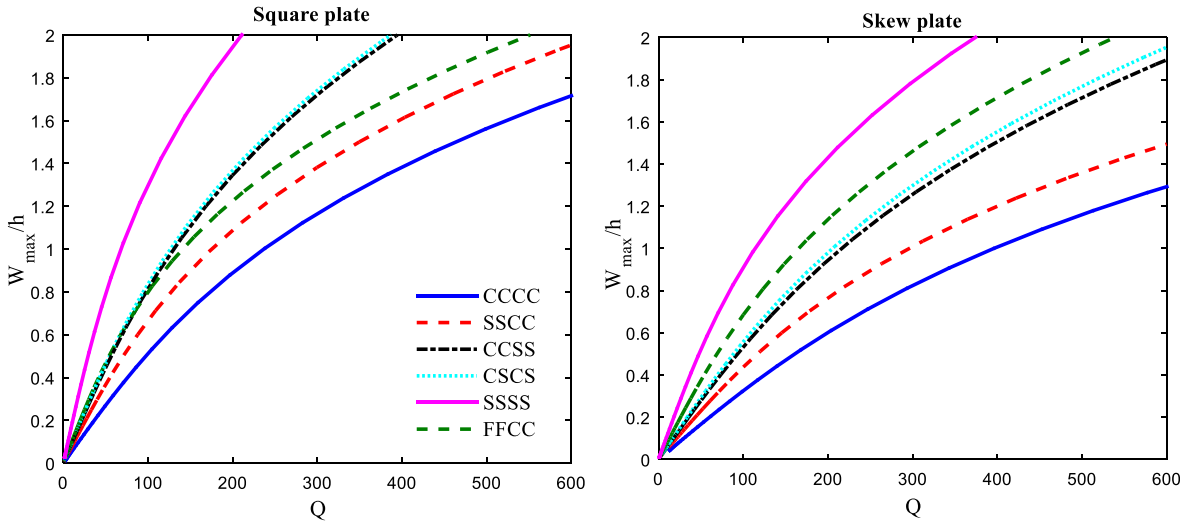

Fig. 14. The effect of boundary conditions on the nonlinear bending response of one-layer cellular square and skew ($\alpha = 30$) plates ($a/h = 20, a/b = 1$).

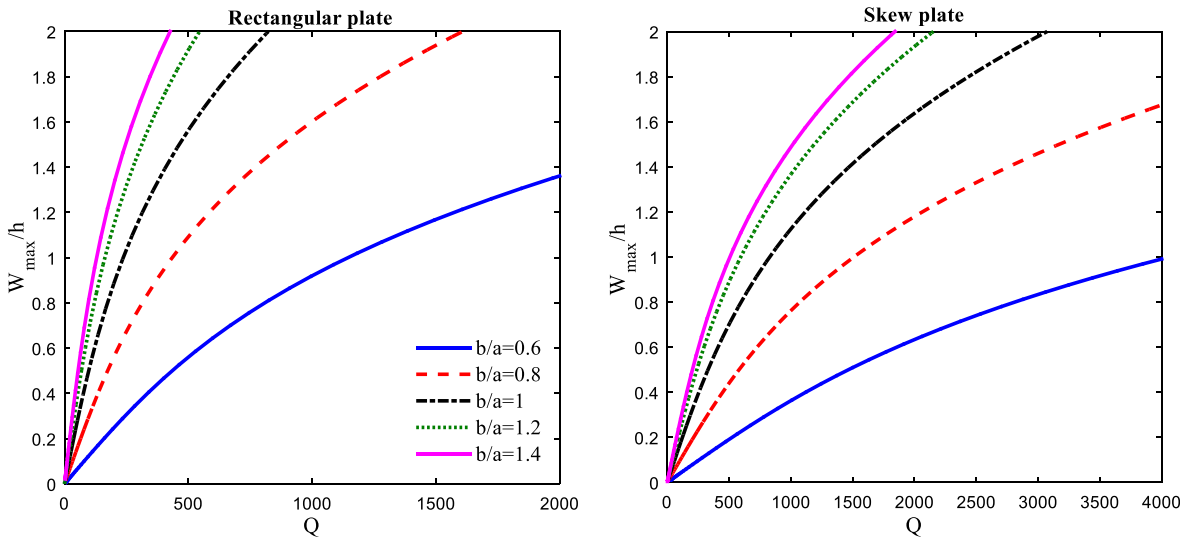

Fig. 15. The effect of the aspect ratio on the nonlinear bending response of fully clamped one-layer cellular rectangular and skew ($\alpha = 30$) plates ($a/h = 20$).

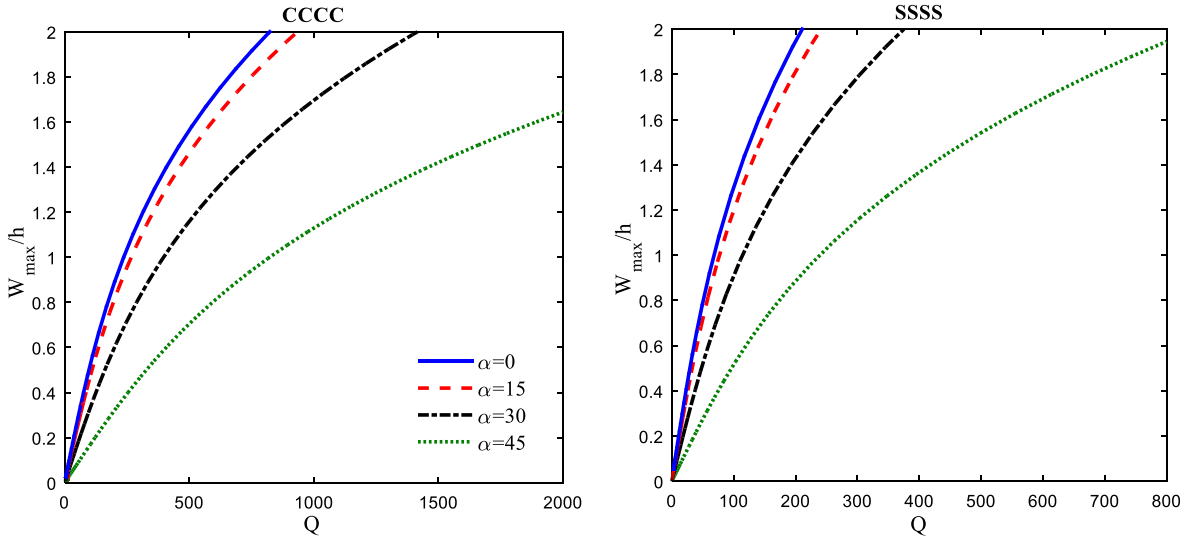

Fig. 16. The effect of the skew angle on the nonlinear bending response of one-layer cellular skew plates ($a/h = 20, a/b = 1$).

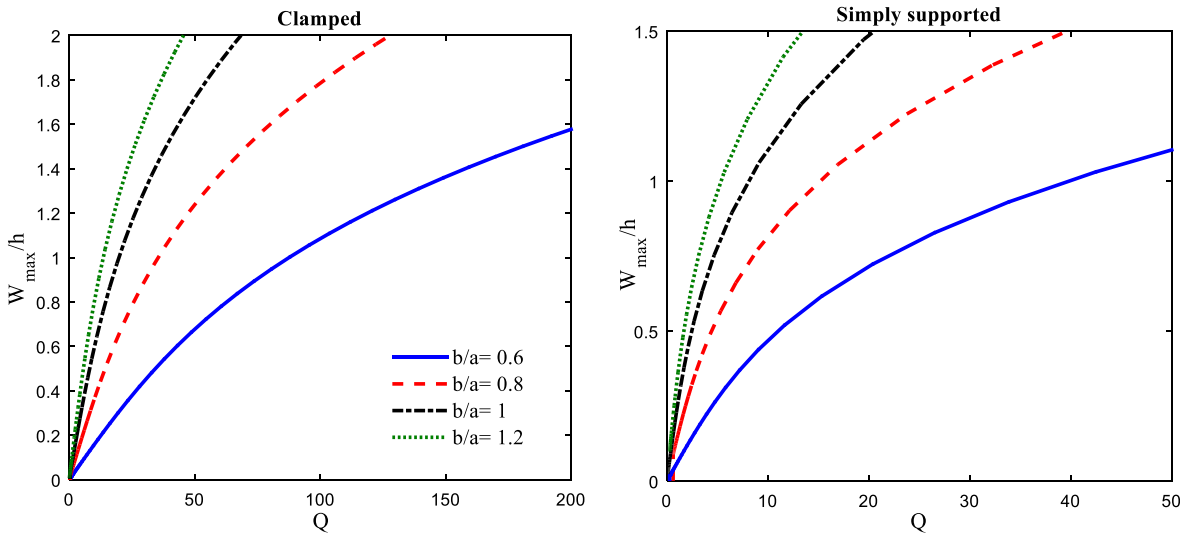

Fig. 17. The effect of the aspect ratio on the nonlinear bending response of one-layer cellular elliptical plates ($a/h = 12$) with fully clamped and fully simply supported boundaries (with the immovable version of the simply supported condition).

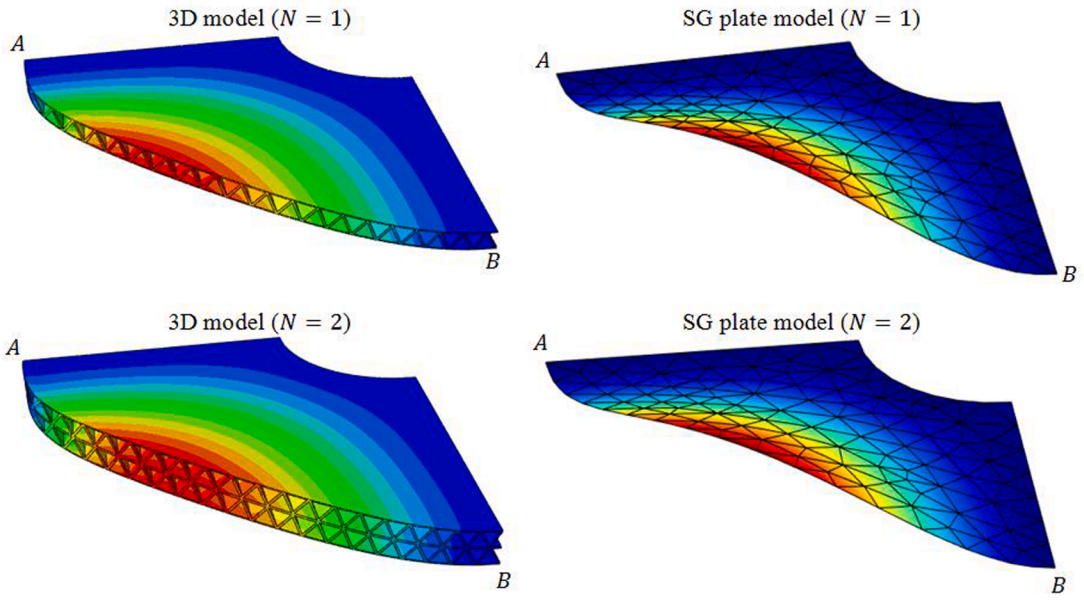

Fig. 18. The normalized distribution of the transversal displacement component of one- and two-layer annular sector plates based on the 3D (reference) model of classical elasticity (left) and the (proposed) strain gradient FSDT (right) with the CCCF boundary condition ($R_2 = 100\text{mm}, R_1/R_2 = 0.3, \alpha = 90$).

values. In fact, by the increase of the sector angle, the plate exhibits a more flexible deformation regime. On the other hand, it is apparent that increasing the radius ratio makes the plate stiffer and decreases the values of the non-dimensional deflection.

5. Conclusions and discussion

The size-dependent geometrically nonlinear bending behavior of cellular plates with equitriangularly prismatic microstructures, or better microarchitectures, was studied within the first-order shear deformation plate theory within the anisotropic strain gradient elasticity theory by employing a higher-order finite element method. Accordingly, this article provided the following novel content: (1) a model derivation, (2) a method development, (3) a method verification, (4) a model validation.

Regarding the theoretical derivations, a matrix–vector form of the appropriate energy functional based on the FSDT plate model and the von Kármán strains within the anisotropic strain gradient elasticity theory was derived. In order to respond to the higher-order continuity requirements resulting from the strain gradient theory, a quasi-C^1-continuous six-node triangular element was developed and the corresponding finite element formulation was presented.

Regarding the computational investigations, in the sense of method verification, the reliability of the proposed finite element method was first confirmed through a numerical convergence study showing the nonstandard method possessing good convergence properties. Then, in the sense of model validation, a variety of comparative results for (reference) 3D full-field models of classical nonlinear elasticity and the (proposed) 2D strain gradient shear deformation plate model was provided in order to approve the accuracy of the proposed approach in case of multi-layer cellular plates with equitriangularly prismatic microstructures. A set of model problems was provided in order to focus, in particular, on the nonlinear size-dependent bending characteristics of the chosen cellular multi-layer plates: it was shown that for small

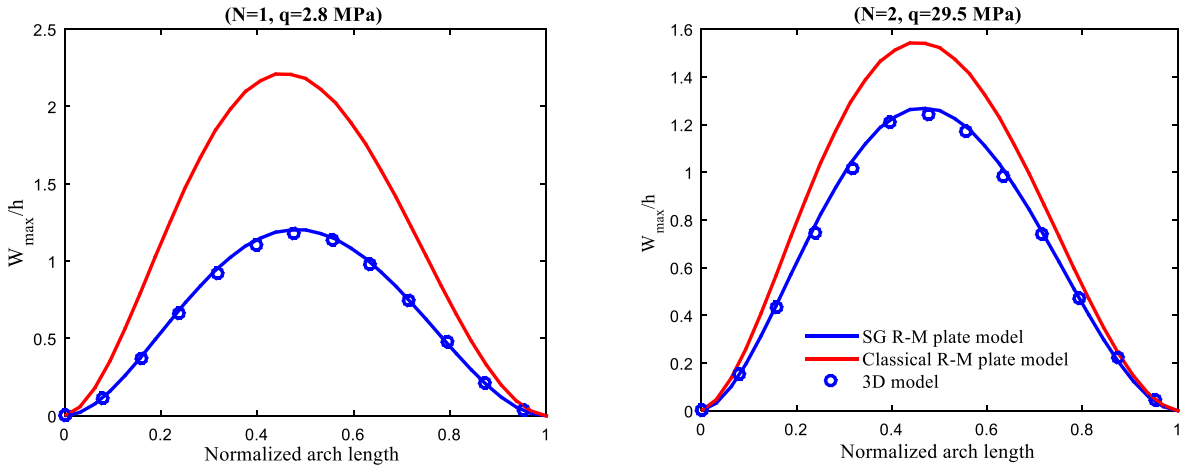

Fig. 19. The non-dimensional maximum deflection of one- and two-layer annular sector plates (left for $N = 1$; right for $N = 2$) along the longer curved edge AB for the CCCF boundary condition ($R_2 = 100\text{mm}, R_1/R_2 = 0.3, \alpha = 90$).

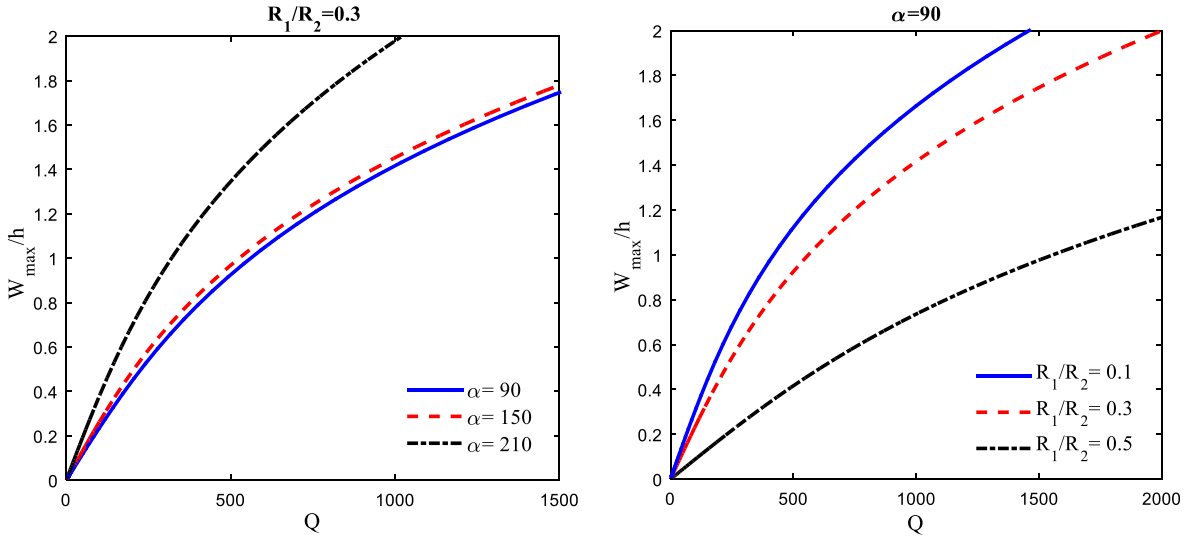

Fig. 20. The effect of the small-to-large ratio of the annular radii (left) and the sector angle (right) on the nonlinear bending response of a fully clamped one-layer ($N = 1$) annular sector plate ($R_2/h = 20$).

numbers of layers, the solutions remarkably differ from the corresponding classical plate solutions but converge towards the classical ones as the number of layers increases. Accordingly, on one hand, the results show a strong interplay between the neighboring scales making the classical plate models useless due to the size effect – or a separate classical model needs to be developed for each layer stack. On the other hand, it was observed that this size effect, or stiffening effect, captured by the proposed strain gradient FSDT for any number of layers, can be relatively small already for three-layer plates, i.e., the results can be quite close to the corresponding results of the classical FSDT. This indicates, perhaps somewhat surprisingly, that the separation of scales does not need to be fully valid for applying the classical continuum theory with rough accuracy. The stiffening effect turned out to be more significant for thinner plates.

As the present study confirms, the proposed model applies within both linear and geometrically nonlinear elasticity for cellular plate structures having an equitriangular lattice core, but we expect the bending phenomenon to be common to other multilayer lattice configurations as well. Indeed, the corresponding beam analyses have been accomplished first for stretching-dominated multilayer triangular lattice beams in [70,71] but very recently for the corresponding bending-dominated square lattice beams in [74]. Therefore, in the subsequent studies, other than equitriangular microarchitectural plates and shells could be investigated, within both linear and geometrically nonlinear regimes. However, when considering the endless possibilities for unit cell geometries it becomes evident that one single generalized model might not be able to cover every possible microarchitecture: even the simplest bending-dominated and stretching-dominated lattice structures might behave differently, not to mention more exotic configurations forming auxetic metamaterials, for instance [59,70,84].

Interestingly, for single-layer sandwich beams and plates the micropolar theory has been applied and calibrated in [80,81] and [82,83], respectively: for single-layer quadrangular (web core) lattice geometries but also for single-layer hexagonal [83], Y-shaped [83], triangular [83] and pyramidic [81] ones – including hence both stretching- and bending-dominated microarchitectures. The corresponding sandwich structures are, however, single-layer structures and repetitions (stacking) of the lattice unit cells do not necessarily produce uniform multi-layer structures made of a periodic lattice metamaterial investigated in the present study and in [7,70–72,74,76,77] – which means that the view of [80–83] is a bit narrower and focuses on specific industrially relevant sandwich configurations. Finally, an interesting study on a single-layer web-core sandwich beam similar to the ones in [80,81] has been accomplished by Barchiesi and Khakalo [85]: in a

global sense, the homogenization procedure therein results, after a condensation, in the classical FSDT beam model which is sometimes considered as a generalized 1D continuum model as such as it already has a rotation degree of freedom.

Regarding other analysis types, already for the present micro-architecture efficient theoretical and numerical modeling for the size effects within elasto-plasticity would open a door to a plethora of applications. Before that, however, free vibration analysis and linear buckling analysis would be natural extensions for the present study, analogously to the corresponding analyses for beam models accomplished in [70] (in this sense, the mathematical form of the strain gradient plate model does not differ from the corresponding classical plate model). In addition, nonlinear thermomechanical bending could be studied by following the linear analyses for beams and plates in [71] and [7], respectively.

Declaration of Competing Interest

The authors declare that they have no known competing financial interests or personal relationships that could have appeared to influence the work reported in this paper.

References

[1] Schaedler TA, Carter WB. Architected cellular materials. Annu Rev Mater Res 2016;46:187–210.
[2] Li Y, Li Z, Yan B, Yan Z. Wind forces on circular steel tubular lattice structures with inclined leg members. Eng Struct 2017;153:254–63.
[3] Fu JY, Wu BG, Wu JR, Deng T, Pi YL, Xie ZN. Design sensitivity analysis for optimal design of geometrically nonlinear lattice structures. Eng Struct 2018;168:915–28.
[4] Prud'homme S, Legeron F, Langlois S. Calculation of wind forces on lattice structures made of round bars by a local approach. Eng Struct 2018;156:548–55.
[5] Nelissen WED, Ayas C, Tekōglu C. 2D lattice material architectures for actuation. J Mech Phys Solids 2019;124:83–101.
[6] Yang H, Ma L. Design and characterization of axisymmetric auxetic metamaterials. Compos Struct 2020;112560.
[7] Khakalo S, Niiranen J. Anisotropic strain gradient thermoelasticity for cellular structures: plate models, homogenization and isogeometric analysis. J Mech Phys Solids 2020;134:103728.
[8] Portela CM, Greer JR, Kochmann DM. Impact of node geometry on the effective stiffness of non-slender three-dimensional truss lattice architectures. Extreme Mech Lett 2018;22:138–48.
[9] Rahali Y, Giorgio I, Ganghoffer JF, dell'Isola F. Homogenization à la Piola produces second gradient continuum models for linear pantographic lattices. Int J Eng Sci 2015;97:148–72.
[10] Meza LR, Phlipot GP, Portela CM, Maggi A, Montemayor LC, Comella A, et al. Reexamining the mechanical property space of three-dimensional lattice architectures. Acta Mater 2017;140:424–32.
[11] Dell'Isola F, Seppecher P, Alibert JJ, Lekszycki T, Grygoruk R, Pawlikowski M, et al. Pantographic metamaterials: an example of mathematically driven design and of its technological challenges. Continuum Mech Thermodyn 2019;31(4):851–84.
[12] Dell'Isola F, Seppecher P, Spagnuolo M, Hayat T. Advances in pantographic structures: design, manufacturing, models, experiments and image analyses. Continuum Mech Thermodyn 2019;31(4):1231–82.
[13] Cosserat E, Cosserat F. Théorie des corps déformables. Paris: Hermann et Fils; 1909.
[14] Eringen AC. Linear theory of micropolar elasticity. J Math Mech 1966;15:909–23.
[15] Eringen AC. Linear theory of nonlocal elasticity and dispersion of plane waves. Int J Eng Sci 1972;10(5):425–35.
[16] Eringen AC. On differential equations of nonlocal elasticity and solutions of screw dislocation and surface waves. J Appl Phys 1983;54(9):4703–10.
[17] Reddy JN. Nonlocal theories for bending, buckling and vibration of beams. Int J Eng Sci 2007;45(2–8):288–307.
[18] Ansari R, Torabi J. Nonlocal vibration analysis of circular double-layered graphene sheets resting on an elastic foundation subjected to thermal loading. Acta Mech Sin 2016;32(5):841–53.
[19] Mindlin RD. Micro-structure in linear elasticity. Arch Ration Mech Anal 1964;16(1):51–78.
[20] Mindlin RD. Second gradient of strain and surface-tension in linear elasticity. Int J Solids Struct 1965;1(4):417–38.
[21] Lam DC, Yang F, Chong ACM, Wang J, Tong P. Experiments and theory in strain gradient elasticity. J Mech Phys Solids 2003;51(8):1477–508.
[22] Niiranen J, Niemi AH. Variational formulations and general boundary conditions for sixth-order boundary value problems of gradient-elastic Kirchhoff plates. Eur J Mech-A/Solids 2017;61:164–79.
[23] Rouhi H, Ebrahimi F, Ansari R, Torabi J. Nonlinear free and forced vibration analysis of Timoshenko nanobeams based on Mindlin's second strain gradient theory. Eur J Mech-A/Solids 2019;73:268–81.
[24] Thai HT, Vo TP, Nguyen TK, Kim SE. A review of continuum mechanics models for size-dependent analysis of beams and plates. Compos Struct 2017;177:196–219.
[25] Andreaus U, Dell'Isola F, Giorgio I, Placidi L, Lekszycki T, Rizzi NL. Numerical simulations of classical problems in two-dimensional (non) linear second gradient elasticity. Int J Eng Sci 2016;108:34–50.
[26] Trovalusci P, Pau A. Derivation of microstructured continua from lattice systems via principle of virtual works: the case of masonry-like materials as micropolar, second gradient and classical continua. Acta Mech 2014;225(1):157–77.
[27] Ansari R, Torabi J. Numerical study on the free vibration of carbon nanocones resting on elastic foundation using nonlocal shell model. Appl Phys A 2016;122(12):1073.
[28] Khakalo S, Niiranen J. Gradient-elastic stress analysis near cylindrical holes in a plane under bi-axial tension fields. Int J Solids Struct 2017;110:351–66.
[29] Ansari R, Torabi J, Faghih Shojaei M. An efficient numerical method for analyzing the thermal effects on the vibration of embedded single-walled carbon nanotubes based on the nonlocal shell model. Mech Adv Mater Struct 2018;25(6):500–11.
[30] Kouris LAS, Bournas DA, Akintayo OT, Konstantinidis AA, Aifantis EC. A gradient elastic homogenisation model for brick masonry. Eng Struct 2020;208:110311.
[31] Matouk H, Bousahla AA, Heireche H, Bourada F, Bedia EA, Tounsi A, et al. Investigation on hygro-thermal vibration of P-FG and symmetric S-FG nanobeam using integral Timoshenko beam theory. Adv Nano Res 2020;8(4):293–305.
[32] Rouabhia A, Chikh A, Bousahla AA, Bourada F, Heireche H, Tounsi A, et al. Physical stability response of a SLGS resting on viscoelastic medium using nonlocal integral first-order theory. Steel Compos Struct 2020;37(6):695.
[33] Yang FACM, Chong ACM, Lam DCC, Tong P. Couple stress based strain gradient theory for elasticity. Int J Solids Struct 2002;39(10):2731–43.
[34] Lazopoulos KA. On the gradient strain elasticity theory of plates. Eur J Mech-A/Solids 2004;23(5):843–52.
[35] Lazopoulos KA. On bending of strain gradient elastic micro-plates. Mech Res Commun 2009;36(7):777–83.
[36] Papargyri-Beskou S, Beskos DE. Static, stability and dynamic analysis of gradient elastic flexural Kirchhoff plates. Arch Appl Mech 2008;78(8):625–35.
[37] Wang B, Zhou S, Zhao J, Chen X. A size-dependent Kirchhoff micro-plate model based on strain gradient elasticity theory. Eur J Mech-A/Solids 2011;30(4):517–24.
[38] Movassagh AA, Mahmoodi MJ. A micro-scale modeling of Kirchhoff plate based on modified strain-gradient elasticity theory. Eur J Mech-A/Solids 2013;40:50–9.
[39] Reddy JN. Theory and analysis of elastic plates and shells. CRC Press; 2006.
[40] Eslami MR. Buckling and postbuckling of beams, plates, and shells. Cham, Switzerland: Springer International Publishing; 2018.
[41] Draiche K, Bousahla AA, Tounsi A, Alwabli AS, Tounsi A, Mahmoud SR. Static analysis of laminated reinforced composite plates using a simple first-order shear deformation theory. Comput Concr 2019;24(4):369–78.
[42] Bourada F, Bousahla AA, Tounsi A, Bedia EA, Mahmoud SR, Benrahou KH, et al. Stability and dynamic analyses of SW-CNT reinforced concrete beam resting on elastic-foundation. Comput Concr 2020;25(6):485–95.
[43] Ansari R, Torabi J, Hassani R. Thermal buckling analysis of temperature-dependent FG-CNTRC quadrilateral plates. Comput Math Appl 2019;77(5):1294–311.
[44] Al-Furjan MSH, Safarpour H, Habibi M, Safarpour M, Tounsi A. A comprehensive computational approach for nonlinear thermal instability of the electrically FG-GPLRC disk based on GDQ method. Eng Comput 2020. https://doi.org/10.1007/s00366-020-01088-7.
[45] Al-Furjan MSH, Habibi M, won Jung D, Sadeghi S, Safarpour H, Tounsi A, Chen G. A computational framework for propagated waves in a sandwich doubly curved nanocomposite panel. Eng Comput 2020. https://doi.org/10.1007/s00366-020-01130-8.
[46] Hirane H, Belarbi MO, Houari MSA, Tounsi A. On the layerwise finite element formulation for static and free vibration analysis of functionally graded sandwich plates. Eng Comput 2021. https://doi.org/10.1007/s00366-020-01250-1.
[47] Ramezani S. A shear deformation micro-plate model based on the most general form of strain gradient elasticity. Int J Mech Sci 2012;57(1):34–42.
[48] Niiranen J, Khakalo S, Balobanov V, Niemi AH. Variational formulation and isogeometric analysis for fourth-order boundary value problems of gradient-elastic bar and plane strain/stress problems. Comput Methods Appl Mech Eng 2016;308:182–211.
[49] Niiranen J, Kiendl J, Niemi AH, Reali A. Isogeometric analysis for sixth-order boundary value problems of gradient-elastic Kirchhoff plates. Comput Methods Appl Mech Eng 2017;316:328–48.
[50] Thai S, Thai HT, Vo TP, Nguyen-Xuan H. Nonlinear static and transient isogeometric analysis of functionally graded microplates based on the modified strain gradient theory. Eng Struct 2017;153:598–612.
[51] Karami B, Janghorban M, Tounsi A. Galerkin's approach for buckling analysis of functionally graded anisotropic nanoplates/different boundary conditions. Eng Comput 2019;35(4):1297–316.
[52] Karami B, Janghorban M, Tounsi A. On pre-stressed functionally graded anisotropic nanoshell in magnetic field. J Braz Soc Mech Sci Eng 2019;41(11):1–17.
[53] Ansari R, Shojaei MF, Mohammadi V, Bazdid-Vahdati M, Rouhi H. Triangular Mindlin microplate element. Comput Methods Appl Mech Eng 2015;295:56–76.
[54] Torabi J, Ansari R, Darvizeh M. A C1 continuous hexahedral element for nonlinear vibration analysis of nano-plates with circular cutout based on 3D strain gradient theory. Compos Struct 2018;205:69–85.
[55] Torabi J, Ansari R, Darvizeh M. Application of a non-conforming tetrahedral element in the context of the three-dimensional strain gradient elasticity. Comput Methods Appl Mech Eng 2019;344:1124–43.
[56] Alimirzaei S, Mohammadimehr M, Tounsi A. Nonlinear analysis of viscoelastic micro-composite beam with geometrical imperfection using FEM: MSGT electro-

magneto-elastic bending, buckling and vibration solutions. Struct Eng Mech 2019; 71(5):485–502.
[57] Balobanov V, Kiendl J, Khakalo S, Niiranen J. Kirchhoff-Love shells within strain gradient elasticity: weak and strong formulations and an H3-conforming isogeometric implementation. Comput Methods Appl Mech Eng 2019;344:837–57.
[58] Balobanov V, Niiranen J. Locking-free variational formulations and isogeometric analysis for the Timoshenko beam models of strain gradient and classical elasticity. Comput Methods Appl Mech Eng 2018;339:137–59.
[59] Niiranen J, Balobanov V, Kiendl J, Hosseini SB. Variational formulations, model comparisons and numerical methods for Euler-Bernoulli micro-and nano-beam models. Math Mech Solids 2019;24(1):312–35.
[60] Thai S, Thai HT, Vo TP, Reddy JN. Post-buckling of functionally graded microplates under mechanical and thermal loads using isogeomertic analysis. Eng Struct 2017;150:905–17.
[61] Torabi J, Ansari R, Bazdid-Vahdati M, Darvizeh M. Second strain gradient finite element analysis of vibratory nanostructures based on the three-dimensional elasticity theory. Iran J Sci Technol Trans Mech Eng 2020;44:631–45.
[62] Yaghoubi ST, Balobanov V, Mousavi SM, Niiranen J. Variational formulations and isogeometric analysis for the dynamics of anisotropic gradient-elastic Euler-Bernoulli and shear-deformable beams. Eur J Mech-A/Solids 2018;69:113–23.
[63] Nguyen HX, Atroshchenko E, Ngo T, Nguyen-Xuan H, Vo TP. Vibration of cracked functionally graded microplates by the strain gradient theory and extended isogeometric analysis. Eng Struct 2019;187:251–66.
[64] Yin S, Chen H, Wu Y, Li Y, Xu J. Introducing composite lattice core sandwich structure as an alternative proposal for engine hood. Compos Struct 2018;201: 131–40.
[65] Al-Furjan MSH, Habibi M, Shan L, Tounsi A. On the vibrations of the imperfect sandwich higher-order disk with a lactic core using generalize differential quadrature method. Compos Struct 2021;257:113150.
[66] Al-Furjan MSH, Habibi M, Ni J, won Jung D, Tounsi A. Frequency simulation of viscoelastic multi-phase reinforced fully symmetric systems. Eng Comput 2020. https://doi.org/10.1007/s00366-020-01200-x.
[67] Shen Y, Cantwell W, Mines R, Li Y. Low-velocity impact performance of lattice structure core based sandwich panels. J Compos Mater 2014;48(25):3153–67.
[68] Polyzos D, Fotiadis DI. Derivation of Mindlin's first and second strain gradient elastic theory via simple lattice and continuum models. Int J Solids Struct 2012;49 (3–4):470–80.
[69] Auffray N, Bouchet R, Brechet Y. Strain gradient elastic homogenization of bidimensional cellular media. Int J Solids Struct 2010;47(13):1698–710.
[70] Khakalo S, Balobanov V, Niiranen J. Modelling size-dependent bending, buckling and vibrations of 2D triangular lattices by strain gradient elasticity models: applications to sandwich beams and auxetics. Int J Eng Sci 2018;127:33–52.
[71] Khakalo S, Niiranen J. Lattice structures as thermoelastic strain gradient metamaterials: evidence from full-field simulations and applications to functionally step-wise-graded beams. Compos B Eng 2019;177:107224.
[72] Khakalo S, Niiranen J. Form II of Mindlin's second strain gradient theory of elasticity with a simplification: for materials and structures from nano-to macro-scales. Eur J Mech-A/Solids 2018;71:292–319.
[73] Tran LV, Niiranen J. A geometrically nonlinear Euler-Bernoulli beam model within strain gradient elasticity with isogeometric analysis and lattice structure applications. Math Mech Complex Syst 2020;8(4):345–71.
[74] Yang H, Timofeev D, Giorgio I, Müller WH. Effective strain gradient continuum model of metamaterials and size effects analysis. Continuum Mech Thermodyn 2020. https://doi.org/10.1007/s00161-020-00910-3.
[75] Romanoff J, Reddy JN. Experimental validation of the modified couple stress Timoshenko beam theory for web-core sandwich panels. Compos Struct 2014;111: 130–7.
[76] Réthoré J, Kaltenbrunner C, Dang TBT, Chaudet P, Kuhn M. Gradient-elasticity for honeycomb materials: Validation and identification from full-field measurements. Int J Solids Struct 2015;72:108–17.
[77] Da D, Yvonnet J, Xia L, Le MV, Li G. Topology optimization of periodic lattice structures taking into account strain gradient. Comput Struct 2018;210:28–40.
[78] Bacigalupo A, Gambarotta L. Generalized micropolar continualization of 1D beam lattices. Int J Mech Sci 2019;155:554–70.
[79] Chowdhury SR, Reddy JN. Geometrically exact micropolar Timoshenko beam and its application in modelling sandwich beams made of architected lattice core. Compos Struct 2019;226:111228.
[80] Karttunen AT, Reddy JN, Romanoff J. Two-scale constitutive modeling of a lattice core sandwich beam. Compos B Eng 2019;160:66–75.
[81] Nampally P, Karttunen AT, Reddy JN. Nonlinear finite element analysis of lattice core sandwich beams. Eur J Mech-A/Solids 2019;74:431–9.
[82] Karttunen AT, Reddy JN, Romanoff J. Two-scale micropolar plate model for web-core sandwich panels. Int J Solids Struct 2019;170:82–94.
[83] Nampally P, Karttunen AT, Reddy JN. Nonlinear finite element analysis of lattice core sandwich plates. Int J Non Linear Mech 2020;121:103423.
[84] Yu X, Zhou J, Liang H, Jiang Z, Wu L. Mechanical metamaterials associated with stiffness, rigidity and compressibility: a brief review. Prog Mater Sci 2018;94: 114–73.
[85] Barchiesi E, Khakalo S. Variational asymptotic homogenization of beam-like square lattice structures. Math Mech Solids 2019;24(10):3295–318.